Palaeogeography, Palaeoclimatology, Palaeoecology 656 (2024) 112579

Contents lists available at ScienceDirect

Palaeogeography, Palaeoclimatology, Palaeoecology

journal homepage: www.elsevier.com/locate/palaeo

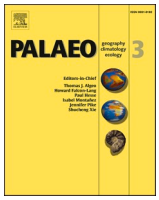

Improved chronostratigraphy and fine-tuned timing for Late Triassic palaeoenvironmental changes in SW Britain using coupled magnetic polarity and carbon isotope stratigraphy

Mark W. Hounslow [a,b,*], Julian E. Andrews [c]

[a] Lancaster Environment Centre, Lancaster University, Lancaster LA1 4YW, UK
[b] Earth, Ocean and Ecological Sciences, Univ. of Liverpool, Jane Herdman Building, Liverpool L69 3GP, UK
[c] School of Environmental Sciences, University of East Anglia, Norwich NR4 7TJ, UK

ARTICLE INFO

Editor: Professor L Angiolini

Keywords:
Magnetostratigraphy
End Triassic extinction
Organic carbon isotope stratigraphy
Norian-Rhaetian boundary
Keuper

ABSTRACT

Understanding the synchronicity of global climatic, environmental, and biotic events around the Norian-Rhaetian boundary (NRB) is problematic because of major international differences in biochronology. We instead use magnetostratigraphic and global carbon isotopic changes to produce more precise global correlation. This work focusses on the base and top of the Rhaetian, with principal age control from a new late Norian to latest Rhaetian magnetostratigraphy from Lavernock (southern Wales) which can be directly correlated to the proposed NRB sections at Pignola Abriola (Italy) and Steinbergkogel (Austria). A disconformity exists in the Lavernock section in its late Norian part (Branscombe Mudstone Formation), but the NRB interval is largely complete. The magnetostratigraphy and a composite $\delta^{13}C_{org}$ stratigraphy from three British sections, demonstrate synchronous changes in both terrestrial and marine records. This analysis indicates the older proposed definition of the NRB from Steinbergkogel is in the upper few metres of the Branscombe Mudstone Formation, while the younger NRB definition from Pignola Abriola is in the upper parts of the Blue Anchor Formation. The latest Rhaetian magnetostratigraphy from Lavernock records reverse magnetochrons UT26r and UT28r which closely pre-date and post-date the widely recognised Marshi and Spelae carbon isotope excursions, respectively. Magnetochrons UT28r and UT27r were previously recognised at St Audrie's Bay (SW England), with relationships to the Newark Supergroup which tightly constrain the first phase of CAMP eruptions to overlap the Spelae excursion. The carbon isotope excursions present in the Blue Anchor Formation lacustrine successions, demonstrate the likely atmospheric, and global spread of these perturbations.

1. Introduction

The pulsed turnover from latest Triassic to earliest Jurassic taxa occur over some ~7 Myr, with changes principally seen around the lower and upper boundaries of the Rhaetian (Jin et al., 2022; Caruthers et al., 2022; McRoberts et al., 2008; Lucas and Tanner, 2018). Understanding the causes of these changes has been hampered by the lack of a robust Rhaetian international timescale; this is due to a paucity of chronostratigraphic markers for subdivision and major regional differences in biochronology from differing faunas and floras. The extinctions and turnovers near the base of the Jurassic have been more intensely studied and are likely linked to pulsed climatic changes caused by the central Atlantic magmatic province (CAMP) flood basalts (Wignall, 2001; Marzoli et al., 2004; Lindström et al., 2017, 2021; Yager et al., 2021); although there are opposing views about the relative timing (Beith et al., 2023).

The faunal turnovers near the base of the Rhaetian have been less well studied and may be linked to several proposed palaeoclimatic changes (Caruthers et al., 2022; Chen et al., 2024). In Upper Triassic continental basins, such as in Britain and the Central European (Germanic) Basin, the interval including the upper Norian to upper Rhaetian is recorded by progressive loss of continental red-bed deposits (formed in arid lacustrine environments; Fig. 1a), and an increasing marine influence (Hounslow and Ruffell, 2006; Bachmann et al., 2010; Barth et al., 2018). In the UK this change is punctuated by increases in shelly faunas associated particularly with the lower parts of the Penarth Group

* Corresponding author at: Lancaster Environment Centre, Lancaster University, Lancaster LA1 4YW, UK.
E-mail address: m.hounslow@lancaster.ac.uk (M.W. Hounslow).

https://doi.org/10.1016/j.palaeo.2024.112579
Received 14 June 2024; Received in revised form 27 October 2024; Accepted 29 October 2024
Available online 3 November 2024

(Fig. 1b), and with open marine faunas by early Hettangian times (Mander et al., 2008; Boomer et al., 2021). The detailed synchronicity of the environmental changes seen in the Central European basins with the better dated marine Rhaetian successions had remained problematic, until magnetostratigraphic and isotopic studies helped better resolve international correlation in the Rhaetian (Hounslow and Muttoni, 2010; Kent et al., 2017; Lindström, 2021). An important issue with the Central European successions is defining the duration and synchronicity of several regional hiatuses which punctuate the Rhaetian shallow marine and lacustrine successions (Lindström and Erlström, 2006; Barnasch, 2009; Bachmann et al., 2010), a situation complicated by the probable diachronous transgression of the marine facies (Barth et al., 2018).

This work addresses two issues. Firstly, establishing a magnetostratigraphy for the Lavernock Point– Penarth cliff sections in South Wales (hereafter referred to as the Lavernock section; Fig. 1a). This allows a better understanding of the regional significance of hiatuses in the UK Rhaetian successions, when integrated with existing English datasets from St Audrie's Bay (hereafter referred to as St Audrie's) and the Seaton-Haven Cliffs (Gallois, 2007, 2009; Hounslow et al., 2004; Hounslow and Gallois, 2023). Secondly, organic carbon isotope data from the lower part of the Rhaetian from these three sections are used to test the potential for refining correlations to marine records: $\delta^{13}C$ records have strong potential for better international correlation in the Rhaetian, as with other intervals in the Triassic (Lucas, 2023).

1.1. Base of the Rhaetian: Uncertainty in its position

How to internationally define the Norian-Rhaetian boundary (NRB) is still debated and complicates detailed studies of the Rhaetian (Fig. 2). The primary boundary marker, the conodont *Misikella posthernsteini* Kozur & Mock 1991 has been proposed in GSSP candidate sections at Steinberkogel (Krystyn et al., 2007) and Pignola Abriola (Rigo et al., 2016) although based on differing characteristics (Galbrun et al., 2020). Fundamentally, this is a disagreement about when this species can be considered a distinct taxon in its evolution from *Misikella hernsteini* Mostler 1978 (Karádi and Korte, 2023; Caruthers et al., 2022). Older (NRB1, at Steinbergkogel; Fig. 1b) and younger (NRB2, at Pignola Abriola; Fig. 2) positions for this boundary have been proposed, with NRB1 supported by other kinds of stratigraphic markers (Krystyn et al., 2007; Krystyn, 2010), and NRB2 being tied to a major negative carbon isotope excursion 50 cm below the presence of this taxon in the Pignola-Abriola section (Rigo et al., 2016). These NRB positions may differ in age by some 2 to 3.5 Myr. At the Austrian NRB1 candidate section at Steinbergkogel, the two definitions of *M. posthernsteini* have first occurrences a few tens of cm from each other (Galbrun et al., 2020). The correlation of the magnetostratigraphy between these sections clearly implicates diachroneity of the taxon definition for NRB2 (Fig. 2). NRB1 is closely associated with the last occurrence of *Monotis salinaria* (Schlotheim 1820) in the uppermost Sevatian, and overlying dwarf monotid faunas at the boundary interval in the base of magnetochron UT23r.1r (Krystyn et al., 2007; McRoberts et al., 2008). In contrast using the last appearance of *Monotis* together with the first occurrence of the conodont *Mockina mosheri* (Kozur & Mostler 1976) morphotype B holds more promise for locating the NRB in North American sections, where *M. posthernsteini* is rare (Lei et al., 2022, 2023). This location for the NRB may approximately correlate to NRB1 (Fig. 2; Krystyn et al., 2007;

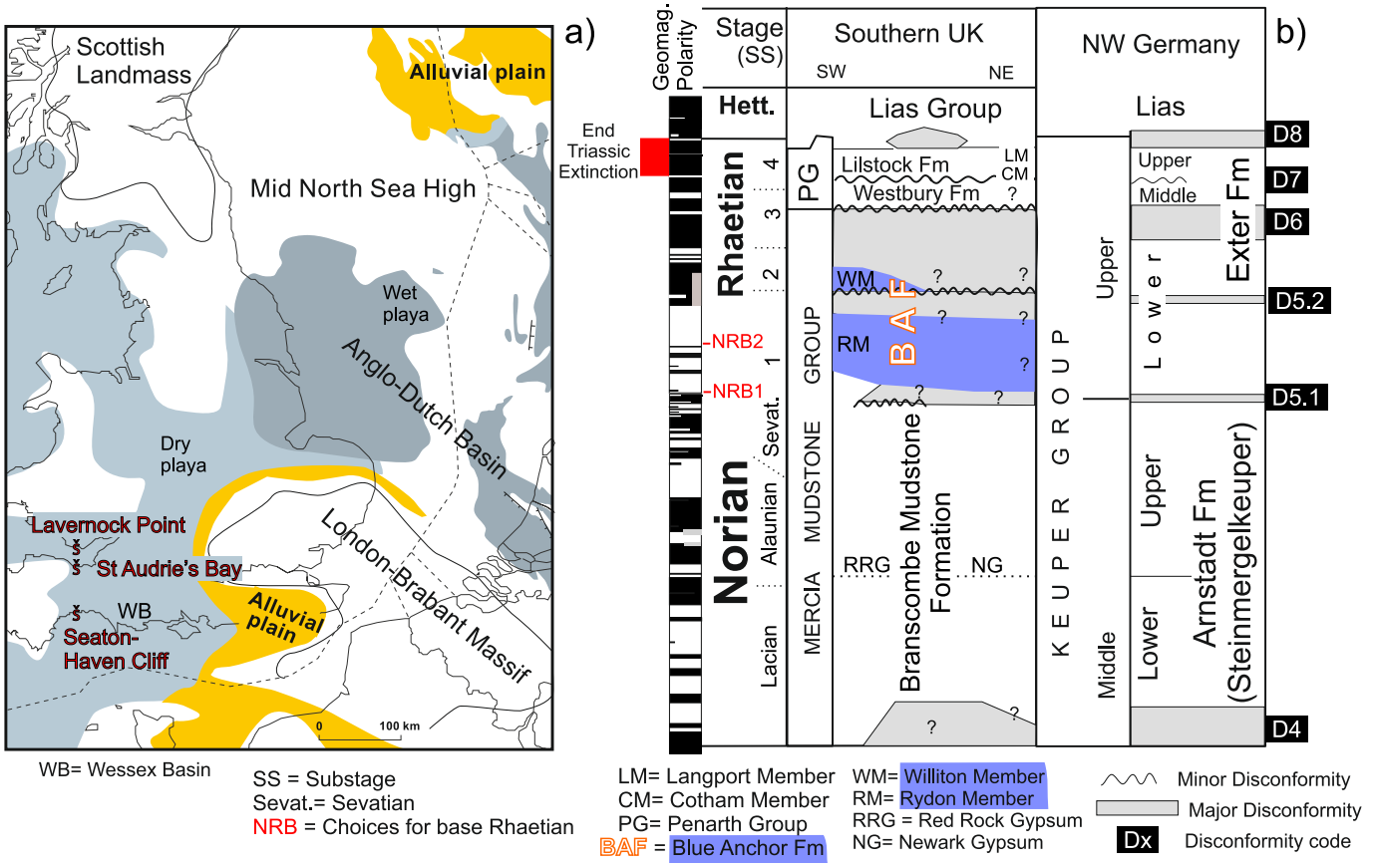

Fig. 1. a) Summary map of locations and environmental facies for the interval occupied by the Branscombe Mudstone Fm, with base map modified from Geluk (2005), using the facies concepts from McKie (2014). B) Summary lithostratigraphy for the Norian- Rhaetian of southern Britain and NW Germany, with regional correlations and disconformities based on Barnasch (2009) and this work. Summary geomagnetic polarity and substage (SS) scale from Hounslow and Gallois (2023). Numbered subdivisions of the Rhaetian based on conodont zones of Krystyn (2008b); with 1 = *bidentata- posthernsteini* Zone. 2 = *posthernsteini -hernsteini* Zone, 3 = *rhaetica* Zone, 4 = *ultima* Zone. Choices for Norian- Rhaetian boundary (NRB1 and NRB2) as in Fig. 2.

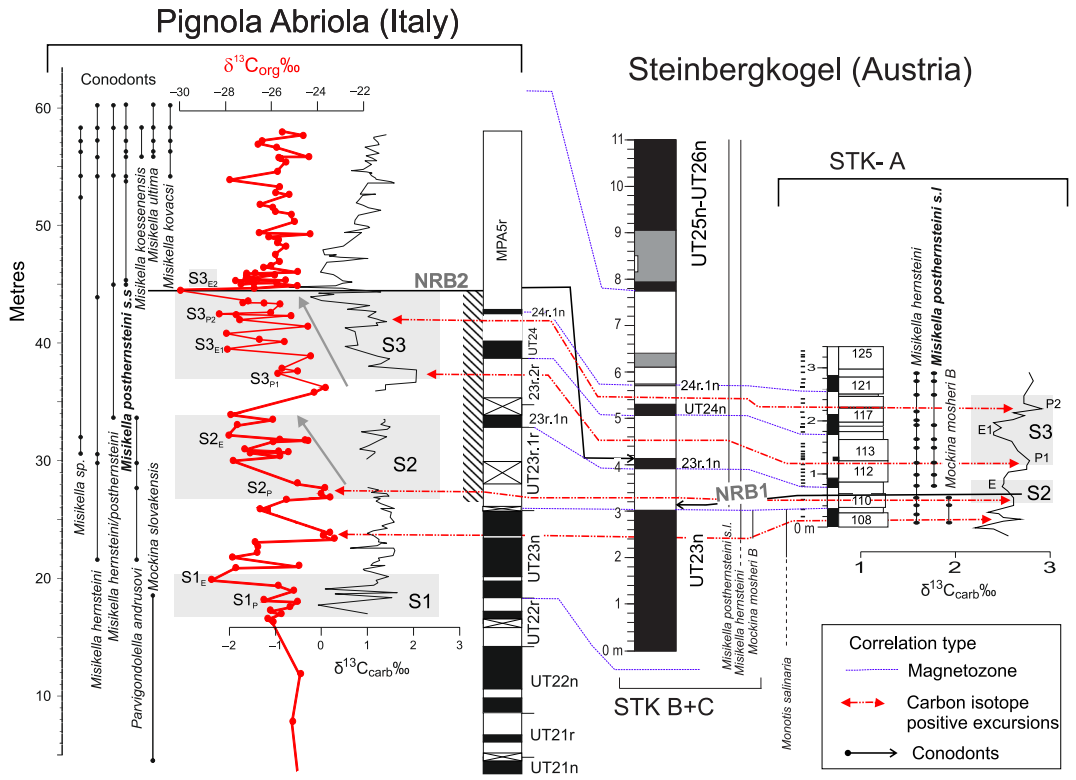

Fig. 2. Summary of linked carbon isotope stratigraphy and magnetostratigraphy across key Norian-Rhaetian boundary sections. Pignola Abriola data from Rigo et al. (2016, 2020), Zaffani et al. (2017, 2018), with intersection correlation proposed by Hüsing et al. (2011). Steinbergkogel data from Krystyn et al. (2007), Krystyn (2008a, 2008b), Hüsing et al. (2011). The proposed boundary positions are NRB1 and NRB2. Magnetozones re-labelled as in the marine Norian-Rhaetian boundary composite in Hounslow and Gallois (2023) adapted here as Fig. 12. Isotope data for section STK-A in Krystyn et al. (2007) was stretched using the bed boundaries into the section/bed thicknesses of Hüsing et al. (2011). Possible coeval isotope excursions shown with red dot-dash lines, and carbon isotope trends (grey boxes) S1, S2 and S3 from Zaffani et al. (2017), with sub-peaks (P) and negative excursions (E) labelled with subscripts. (For interpretation of the references to colour in this figure legend, the reader is referred to the web version of this article.)

Krystyn, 2008b).

What could be global carbon isotope excursions at the NRB (Fig. 2), appear at three intervals (S1 to S3; Zaffani et al., 2017, 2018; Rigo et al., 2020), although the critical youngest, S3, is currently only well expressed in a few datasets (Zaffani et al., 2018; Jin et al., 2022). These negative carbon isotope excursions at around the NRB2 position have not been universally identified in other sections, although this could be due to problems with precise correlation (Caruthers et al., 2022; Karádi and Korte, 2023; Rizzi et al., 2020; Lei et al., 2023). Using the magnetostratigraphy for correlation between the two candidate sections, it is plausible that the carbon isotope changes at Pignola Abriola have coeval $\delta^{13}C_{carb}$ changes at Steinbergkogel, although suppressed in magnitude (Fig. 2).

2. The Lavernock Point to Penarth sections: Synthesis and new field observations

The cliff and foreshore exposures at and east of Lavernock Point (near Penarth), expose an Upper Triassic succession (Richardson, 1905; Ivimey-Cook, 1974; Waters and Lawrence, 1987; Warrington and Ivimey-Cook, 1995) starting in the Norian aged upper Mercia Mudstone Group (Branscombe Mudstone and Blue Anchor formations; Figs. 3, 4) through the upper Rhaetian Penarth Group (Westbury and Lilstock formations) into the base of the Jurassic Lias Group (Fig. 5). This succession records a progressive change from continental lacustrine and floodplain mudstones with evaporites (Branscome Mudstone Fm) into increasingly marine-influenced playas (Blue Anchor Fm) through to fully marine and marginal marine/brackish seas (Penarth Group). This study is based on a new measured section through the Branscombe Mudstone Fm (Fig. 3). The measured sections in the Blue Anchor Fm and Penarth Group (Figs. 4 and 5) are based on Waters and Lawrence (1987).

2.1. Branscombe Mudstone Formation (Mercia Mudstone Group)

The cliffs and foreshore at Lavernock expose the upper 20 m of the Branscombe Mudstone Fm (Waters and Lawrence, 1987; Warrington and Ivimey-Cook, 1995). The dominant lithology is a silty, dolomitic red mudstone, although green coloured mudstone beds, or green mottles, are common. The mudstones are non-fossiliferous (Warrington and Ivimey-Cook, 1995) but contain both nodular and vein-hosted gypsum, and/or nodular celestite (Fig. 3). The nodular gypsum can attain thicknesses of 30–40 cm and often display a cm-wide halo of green coloured mudstone. Celestite nodules are typically around 10 cm diameter and become more common than gypsum in the upper 4 m of the formation (Fig. 3). Prominent nodular vugs (former gypsum nodules) may be present in the celestite-bearing mudstones. Low-angle cross bedding and lenticular fine-grained sandstones are present ~2 m below the top of the formation (~20 cm below sample LP37) at a level of disconformity with a very shallow angle of truncation (Fig. 3). A few horizons show peloids, and recently a sauropod track (Hartley and Shuttleworth, 2024) has been found close to the base of the measured section.

The Branscombe Mudstone Fm at Lavernock represents evaporitic lacustrine and alluvial flat environments traversed by sauropods; the sulphates precipitated out of saline groundwater. Some of the nodular gypsum shows chicken-wire textures, probably after primary depositional anhydrite (Alan Kendall pers. comm.). The low angle cross-bedding is contained in shallow channels or sheetwash deposits which have locally eroded the underlying sediments under shallowing-upward conditions. The peloids may indicate localised soil-zone processes, or

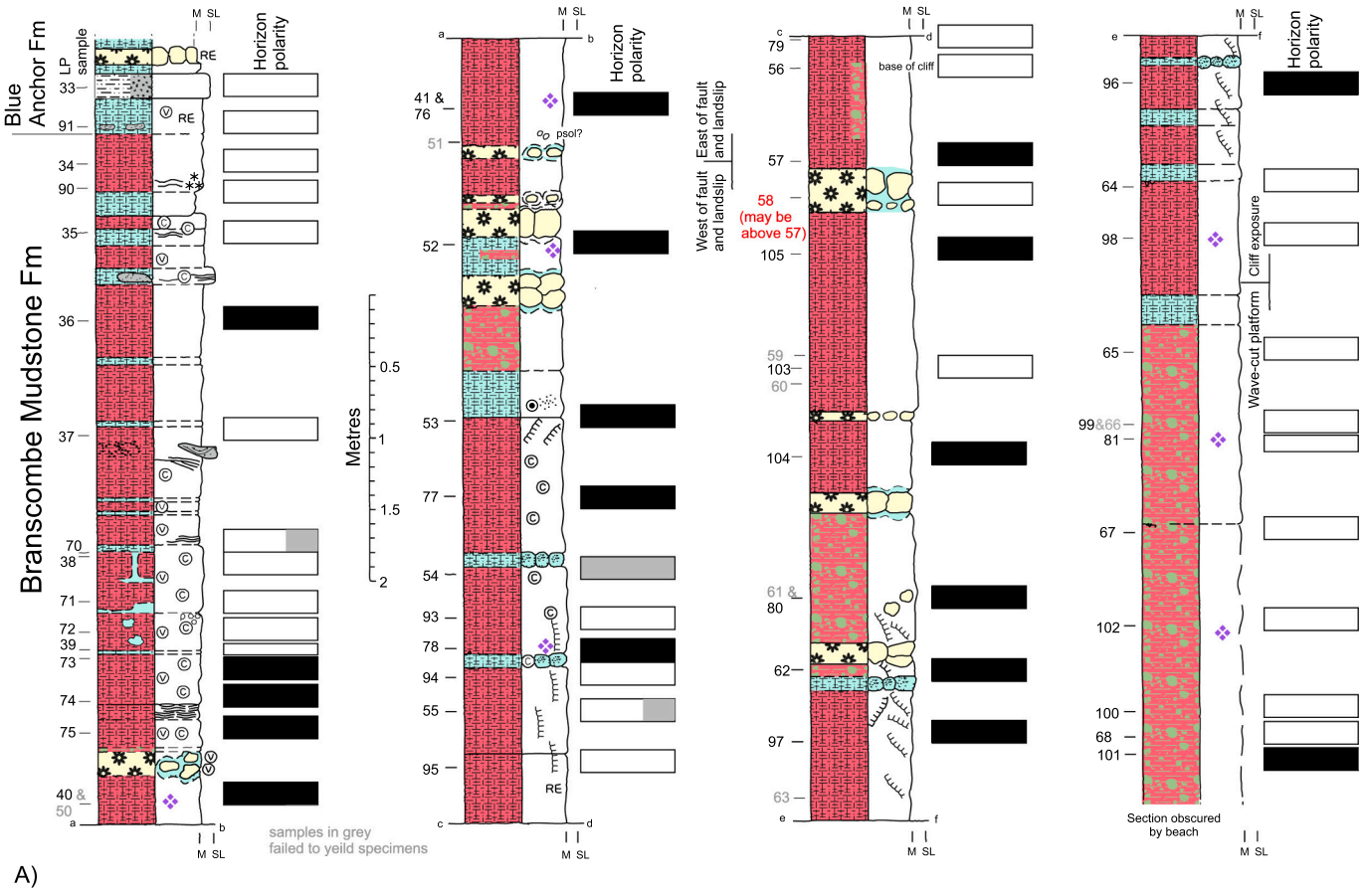

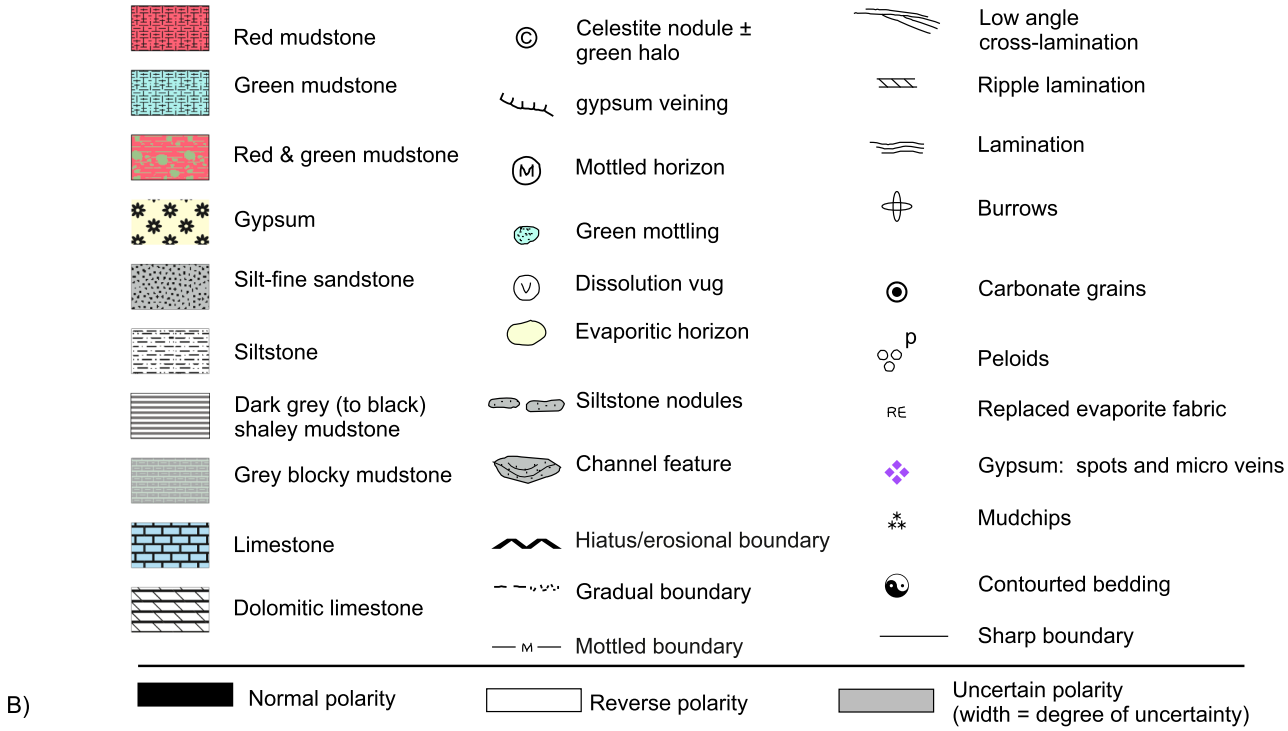

Fig. 3. A) Sedimentary log of the Branscombe Mudstone Fm and basal Blue Anchor Fm in the Lavernock Point to Penarth section, and the geomagnetic polarity of the sampled horizons (LP sample numbers on left of log). M = mudstone, SL = siltstone, a–b, c–d, e–f are matching levels in adjacent columns. B) Key to the sedimentary logs, and geomagnetic polarity. (For interpretation of the references to colour in this figure legend, the reader is referred to the web version of this article.)

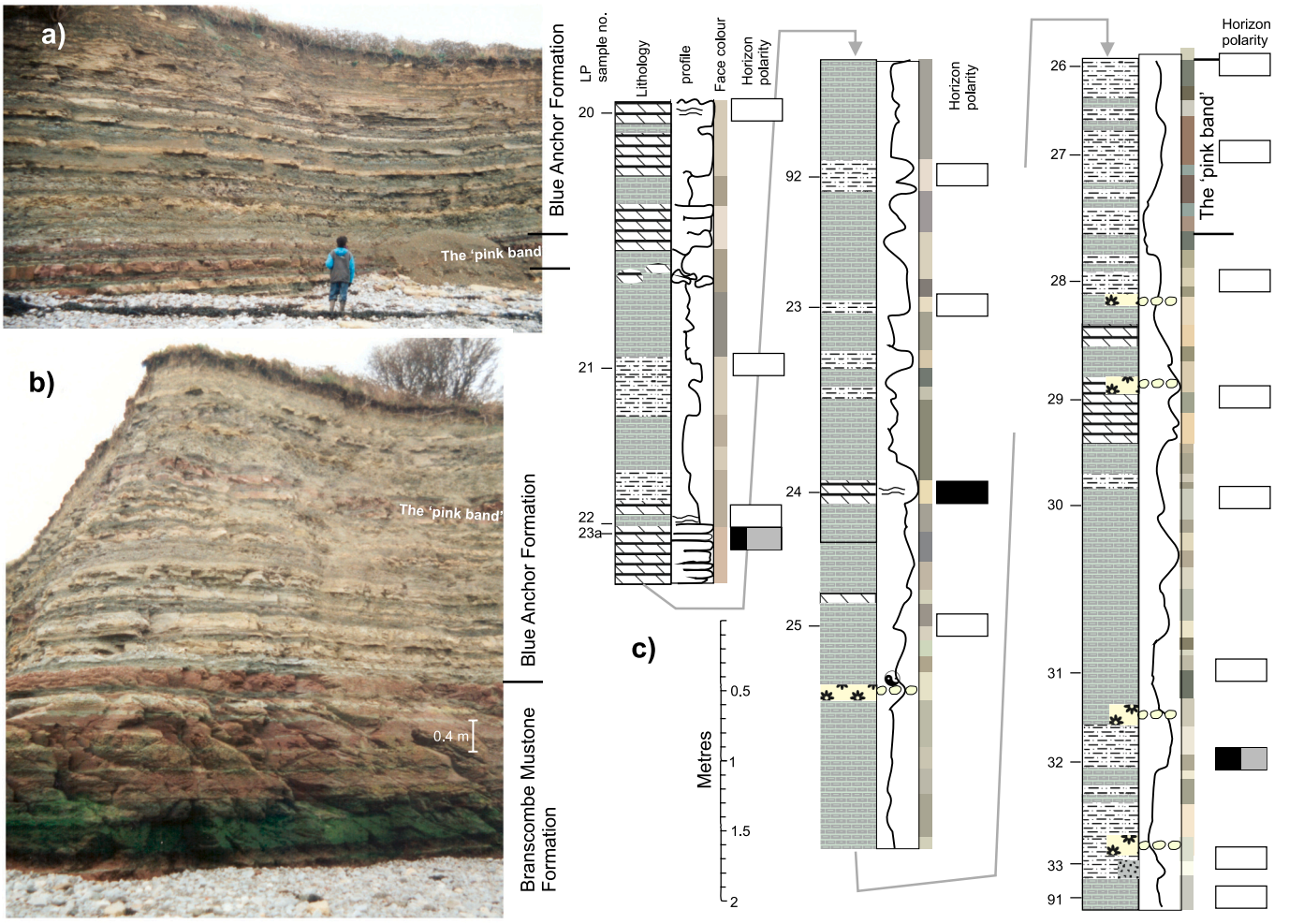

Fig. 4. A), b) The Blue Anchor Formation at Lavernock and c) sedimentary log of the Blue Anchor Fm at Lavernock Point (log modified from Waters and Lawrence, 1987), with polarity of the sampled horizons. See Fig. 3b for key to log. (For interpretation of the references to colour in this figure legend, the reader is referred to the web version of this article.)

perhaps some mud transportation as aggregates, as in modern arid settings (Magee et al., 1995).

2.2. Blue Anchor Formation (Mercia Mudstone Group)

At Lavernock the Blue Anchor Fm is 15 m thick and represented entirely by the Rydon Mb of Mayall (1981); the base is sharp, defined by the first grey-green more thinly bedded mudstone (Fig. 4). Mudstone dominates but 20 cm thick argillaceous dolostones and limestones become more common upward (Warrington and Ivimey-Cook, 1995). Gypsum nodules are again common in the lower part and a prominent 1.2 m thick red mudstone (the 'pink-band' of Waters and Lawrence, 1987) is a convenient marker horizon (Fig. 4). Mudcracks, intraclasts and simple burrows are present and vertebrate tracks occur ~5 m below the top of the formation (Falkingham et al., 2022). Overall, the Blue Anchor Fm at Lavernock broadly represents a regionally traceable (Hounslow and Ruffell, 2006) transition from evaporitic alluvial flats, through evaporative, semi-permanent lakes, to marginal marine muds in the overlying basal Westbury Fm. The red mudstone of the 'pink-band' suggests a brief resumption of drier alluvial-mudflat conditions as seen in the Branscombe Mudstone Fm.

2.3. Westbury and Lilstock formations (Penarth Group)

The Penarth Group is around 11 m thick and has an erosive, unconformable lower contact with the Blue Anchor Fm, at the base of the Westbury Fm (Mayall, 1981). The Westbury Fm is characterised by dark shales with decimetre thick sandstones and limestones arranged into six persistent depositional cycles in South Wales (Ivimey-Cook, 1962, 1974). These start with fine-grained sandstones that fine upward into shales with marine bivalves. The Westbury Fm represents broadly shallow marine deposition, with the coarse clastics deposited during storms, and/or by transgressive lags reworking phosphatised near-shore material (MacQuaker, 1994; Suan et al., 2012).

The Lilstock Fm (Penarth Group) overlies the Westbury Fm with a prominent channelised erosion surface marking the base of the Cotham Mb; green-grey calcareous mudstones and wave ripple marked thin siltstones and limestones follow with marine fossils present (Fig. 5a). The lower Cotham Mb ends with a 15 cm thick mudstone displaying prominent synsedimentary deformation (micro faults and slump folds). The basal beds of the upper Cotham Mb include a thin oolitic sandstone that fills large desiccation cracks, some of which penetrate to the top of the Westbury Fomation. Wavy bedded calcareous mudstone and siltstones follow, these lack macrofossils but foraminifera and ostracods indicate a schizohaline environment. The overlying Langport Mb begins with 0.65 m of porcellanous limestones (porous micritic limestones) with marine bivalves (Langport beds or White Lias facies; Gallois, 2009), passing upward into ~2 m of grey calcareous mudstones again with marine bivalves (Watchet Beds; Fig. 5a). Paper shales of the Hettangian Blue Lias facies rest sharply on the uppermost Watchet Beds. The

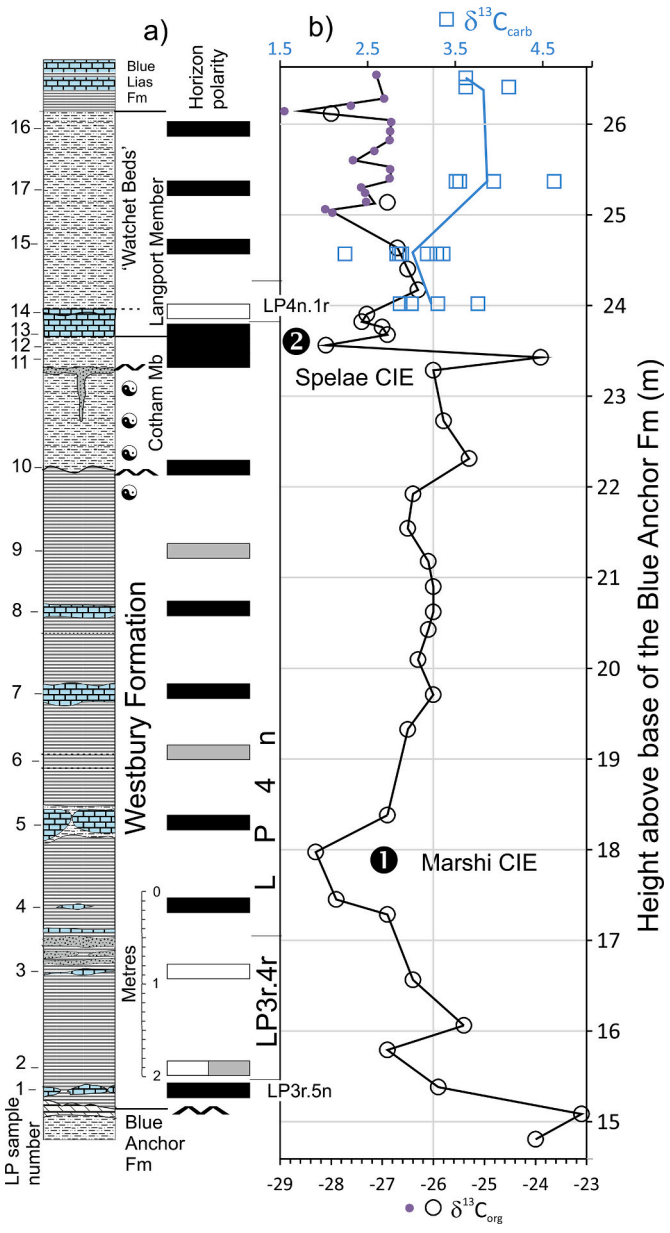

Fig. 5. a) The sampling (LP sample code), sedimentary log and geomagnetic polarity of the Penarth Group at Lavernock (log adapted from Waters and Lawrence, 1987). b) $\delta^{13}C_{org}$ data from Suan et al. (2012) (open circles) and Beith et al. (2021) (smaller filled circles), and $\delta^{13}C_{carb}$ from Korte et al. (2009) (squares). The isotope data were mapped onto the section log using the lithologies, not directly the meter heights, which differ slightly between these studies. The Marshi and Spelae Isotope excursions of Lindström et al. (2017) are labelled with ❶ and ❷. Both a) and b) have equivalent meter divisions. Key to the log in Fig. 3b.

Lilstock Fm (Penarth Group) mostly represents shallow, inshore, transgressive, marine deposits, generally connected to the open ocean but at times more closed off to form the lagoonal deposits of the Cotham Mb. Horizons of synsedimentary deformation and desiccation cracking in the Cotham Mb may be traceable throughout the Bristol Channel Basin (Gallois, 2009), with the deformation likely caused by seismic events, possibly linked to CAMP-related tectonism (Laborde-Casadaban et al., 2021).

3. Sampling and Laboratory Methods

Oriented hand samples were collected with reference to the measured sections, with vertical sample spacing not more than 0.5 m, but guided by bed thickness and lithology/facies variation. Sample orientations were measured using a purpose-designed surface orientation staff (Hounslow et al., 2022a). The samples were subsequently re-oriented and mounted in plaster, with the oriented surface horizontal. Specimens were cut from these blocks, mostly dry on a diamond saw, since the mudstones were prone to disintegration in water. Tilt tests were not possible due to low dispersion in the shallow bedding dips (of 2-12°). Selected sub-samples were used for organic carbon isotope analysis.

3.1. Magnetic methods

The natural remanent magnetisation (NRM) of 181 specimens was measured with GM400 3-axis squid magnetometer, with removal of the residual holder magnetisation (holder mean ~ 0.35×10^{-10} Am^2) and estimation of directional precision using the γ_{95} of Briden and Arthur (1981) with 12 measurements of each X, Y, Z, using three specimen positions. The practical measurement floor was around 3 μA/m. For this sample set, median γ_{95} is 8.2° with 29 % of measurements having $\gamma_{95} >$ 15°. A subset (37) of the stronger specimens was measured on a JR5 spinner magnetometer. Thermal demagnetisation was effective on the red and reddish mudstones (up to ~650-710 °C; Supplementary Information (SI) Fig. S7). A combined scheme was used on the grey and green lithologies (magnetite-dominated magnetisations) with thermal demagnetisation (up to ~200-350 °C), followed by reversing-tumbling AF demagnetisation up to 80 mT. The same procedure was used by Hounslow et al. (2004), Hounslow and Gallois (2023) and Hüsing et al. (2014) on rocks from the same formations. A Magnetic Measurements Ltd. MMTD1 (with field cancellation generally <5nT) was used for thermal demagnetisation and a Molspin Ltd. demagnetiser for AF demagnetisation. Specimens were kept in zero-field Mu-metal boxes between heating steps to limit viscous remanence acquisition caused by thermal alteration, which was monitored by magnetic susceptibility (K) measurements. The red-mudstones samples had particularly strong short-term viscous magnetisations, with many also showing major increases in K around 500 °C (SI Figs. S4- S6).

The demagnetisation data were analysed with the LINEFIND software (Kent et al., 1983), a more sophisticated version of the standard principal component analysis. The demagnetisation behaviour and nature of characteristic remanence was classified into either line-fits (S-class behaviour) or great circle trends (T-class behaviour, fitted to a great circle plane). In each case the degree of scatter was sub-divided into three qualitative classes (T1 to T3, and S1 to S3), with T1 and S1 having the least scatter and being most well defined, and S3 and T3 the most scatter and least-well defined. A demagnetisation class of X was used for specimens which were either very scattered, insufficiently demagnetised, or were inferred to have no characteristic remanent magnetisation (ChRM). The inferred polarity was similarly divided into three quality categories for reverse (R, R? and R??) and normal polarity (N, N?, N??). A last polarity category of U was used for specimen data in which the polarity could not be confidently assigned. Details of this categorisation can be found in Hounslow et al. (2004) and Hounslow and Gallois (2023). Directional analysis used the PmagTools software (Hounslow, 2023).

Magnetic mineralogy of the whole section was not investigated in detail and is assumed to be like the same formations investigated by Hounslow (1985), Hounslow et al. (2004), Hüsing et al. (2014) and Hounslow and Gallois (2023). An inter-section comparison of the NRM intensity and magnetic susceptibility of these formations is shown in SI Fig. S1. A single red-mudstone sample from the Branscombe Mudstone (LP55; Fig. 3a) was investigated by Maher et al. (2004) with low temperature methods and shown to contain largely fine-grained hematite like other similar UK red-beds (SI Fig. S2).

A small sub-set of specimens (from LP1,5,7,8,12,13,14,17; from the Penarth Group; Fig. 5a) was investigated with rotational remanent

magnetisation (RRM) methods (Hounslow et al., 2023), using a 2G RAPID magnetometer. RRM is related to the mechanisms of gyroremanent magnetization acquisition and is acquired when samples are rotated in an alternating magnetic field (Wilson and Lomax, 1972; Potter and Stephenson, 1986; Mahon and Stephenson, 1997). The RRM produced is either parallel or antiparallel to the rotation vector, and for magnetite is preferentially acquired by single domain particles (Potter and Stephenson, 1986). Hematite does not acquire RRM, but pyrrhotite and greigite do. This sample-set was investigated, since there is uncertainty in the contribution of magnetic sulphides to the magnetisation in the Penarth and Lias Groups (Hounslow et al., 2004; Hüsing et al., 2014), and RRM methods are particularly sensitive for distinguishing magnetic sulphides from magnetite (Snowball, 1997). The magnitude and sign of RRM is expressed as the Bg parameter (Potter and Stephenson, 1986). Also utilised are the static (i.e. the conventional form) anhysteretic remanent magnetisation (ARM), the rotational ARM (ARM_{ROT}) at rotation rates of 2.5 Hz and 0.262 Hz, and the percentage of static ARM remaining after static 40 mT demagnetisation ($d.ARM_{40mT}$). These provide a set of mineral-diagnostic proxies (Hounslow et al., 2023; Fig. 6). A static AF field of 100 mT was used with ARM_{ROT}, ARM and RRM (peak AF hold time, 92 ms). The DC field used for ARM and ARM_{ROT} was 100 μT. For the RRM an AF hold time of 962 ms was used, the optimum proposed by Hounslow et al. (2023) for the demagnetising system of the RAPID magnetometer.

Options for polarity correlations were quantitatively assessed for statistical similarity with the similarity of matrices index (SMI), Procrustes similarity index (PSI) and distance correlation (dCor) statistics (Székely and Rizzo, 2017; Indahl et al., 2018). These multivariate statistics used five variables to characterise magnetozones/chrons: t_0 (thickness, or duration) of the magnetozone, geometric mean of t, $\log_e(t_{-1}/t_0)$, polarity bias, Shermans ω_2 statistic. These use, t_{+1}, t_{-1}, the corresponding values for the underlying and overlying magnetozones and t_0, metrics that are less dependent on sedimentation rate changes (Man, 2008). The polarity bias, ω_2 and geometric mean metrics characterise more about the local polarity structure than using t_0 or $\log_e(t_{-1}/t_0)$ individually (Olson et al., 2014) and have been used in other quantitative multivariate polarity correlation assessments (Man, 2008; Hounslow et al., 2022a). The probability of association of the corresponding polarity patterns uses the RV-based statistic P_{RV}, and permutation test for dCor giving P_{dCor} (Székely and Rizzo, 2017; Josse and Holmes, 2016). Lastly the divergence of magnetozone characteristics in the correlation models were characterised by the Euclidean distance (d_i, using the above five metrics above). Care was taken to standardize the five metrics. The packages MatrixCorrelation, dCor and FactoMineR were used in R for this assessment (R Core Team, 2022). Datasets and R-scripts are given in the Figshare repository (Hounslow, 2024).

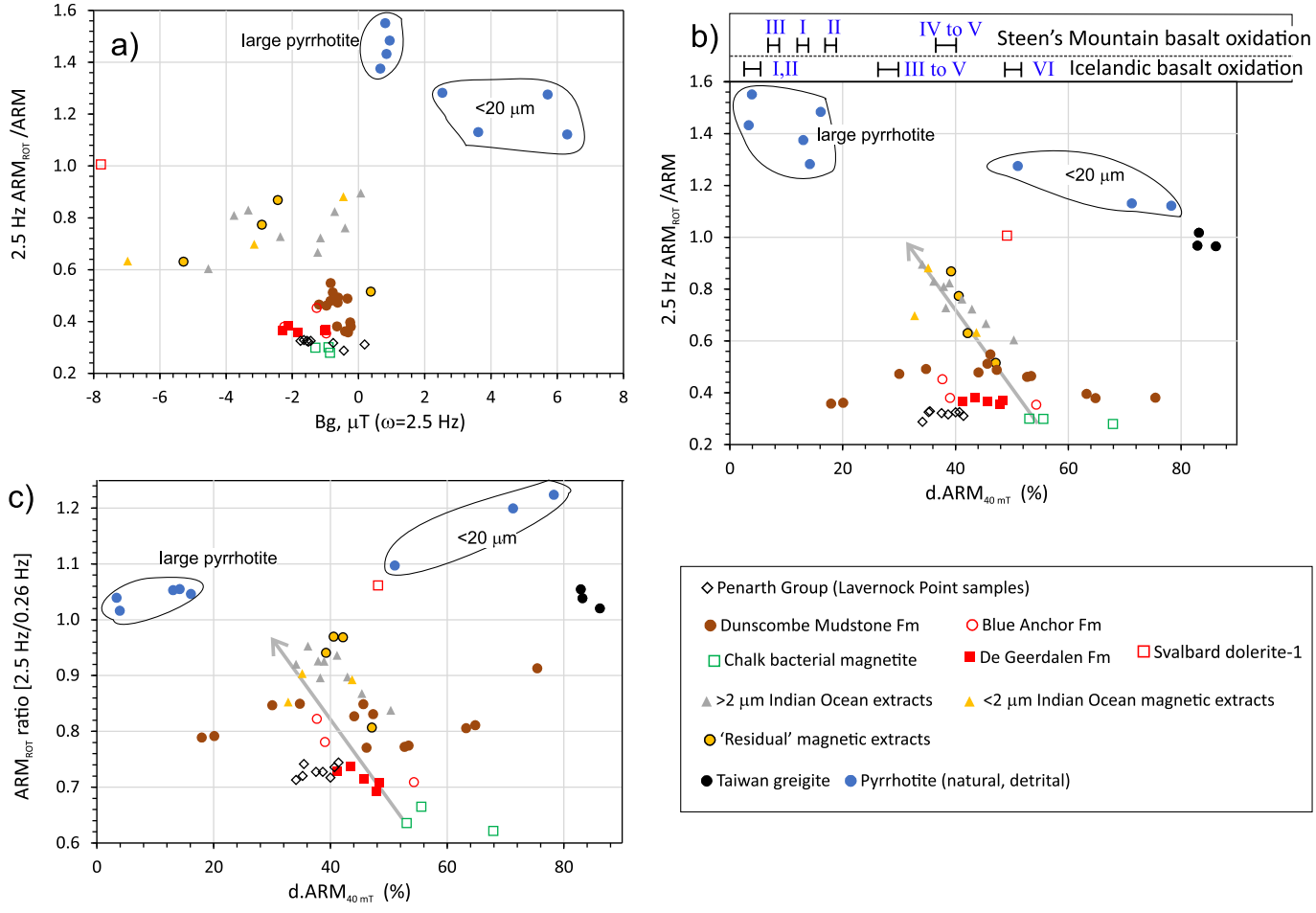

Fig. 6. Summary rock magnetic data for the Lavernock samples, compared to the set of well characterised reference materials in Hounslow et al. (2023). a), b) and c) relate to the same parameterized reference datasets as in figs. 14a, 14b and 14d in Hounslow et al. (2023). Additionally, comparable data for non-red samples in the Dunscombe Mudstone and Blue Anchor formations from the South Devon coast (Hounslow and Gallois, 2023) are show for comparison. Dataset listed in Hounslow (2024). In b) the top of the panel shows the range of $d.ARMz_{40mT}$ values for the petrological oxidation states I to VI (Watkins and Haggerty, 1967) of basalts from the Steen's Mountain and Icelandic basalts (from Dunlop, 1983). Grey arrows in b) and c) shows the likely progression to multidomain type behaviour, from SD-like behaviour at low ARM_{ROT}/ARM and ARM_{ROT} (2.5 Hz/0.26 Hz) ratio. For all these data the RRM was measured with an AF hold time of 962 ms. Rotation rate = ω in Hz. (For interpretation of the references to colour in this figure legend, the reader is referred to the web version of this article.)

3.2. Organic carbon isotope method

A sub-sample from selected palaeomagnetic samples was measured for $\delta^{13}C_{org}$. Around 20 g of sub-sample was powdered in a ball mill, and carbonate minerals were removed by reacting the homogenised material with 6 N HCl at 25 °C for 24 h, which removes dolomite, siderite and ankerite (Brodie et al., 2011). After reaction-ceased, residues were washed several times with distilled water to remove any traces of acids. Residues were then oven-dried at 50 °C for 24 h and subsequently re-powdered prior to $\delta^{13}C_{org}$ isotope analysis. Decarbonated residues were weighed into tin capsules and loaded into an auto-sampler connected to an Elementar Vario MICROcube, from where they were dropped into the furnace at 950 °C. Produced gases were passed (under He) through chemical traps to remove sulphur, excess oxygen, and water. Large sample masses were used to enable reliable measurements of $\delta^{13}C_{org}$ down to around 0.02 % total organic carbon. Percent total carbon (%TOC) and total nitrogen (%N_T) were measured with a precision of ~0.01 %. Nitrogen was separated from CO_2 by temperature programmed desorption. The isotopic composition of the resultant purified CO_2 was then measured using an Isoprime100 Isotope mass spectrometer. Carbon isotope ratios are reported as delta values ($\delta^{13}C$) in per mil relative to the international VPDB scale (standards used: NBS-18 = −5.014 ‰; LSVEC = −46.6 ‰). Analytical precision (1σ) is estimated to be ±0.15 ‰ for $\delta^{13}C_{org}$ based on the replicate analysis of pure, well-mixed, organic compounds used as laboratory calibration materials.

4. Results

4.1. Magnetic mineralogy

The NRM intensity and magnetic susceptibility show a broad partition into the more strongly magnetic red mudstones in the Branscombe Mudstone Fm and weaker magnetic properties in the Blue Anchor Fm and Penarth Groups (Fig. 7b; SI Fig. S1). This is apart from larger NRM intensity in the 'Pink Band' (~ +6 m; Fig. 7b) of the Blue Anchor Fm, and LP20 (15.12 m; Fig. 4) in the top of the Blue Anchor Fm.

The RRM measurements of samples from the Penarth Group all show (except one sample; LP5) small negative Bg values (Fig. 6a). These are typical of reference natural magnetite materials, and unlike the large negative Bg of greigite and the positive Bg values of pyrrhotite (Snowball, 1997; Hounslow et al., 2023). The d.ARM_{40mT} of the Lavernock samples show a tight grouping near to reference material with oxidized magnetite as seen in other siliciclastic Triassic sediments (Fig. 6b). The low ARM_{ROT}/ARM ratio of these is clearly distinct from reference greigite and natural pyrrhotite (Fig. 6b). Fully multidomain (MD) behaviour in magnetite should give Bg = 0 (Potter and Stephenson, 1986), and d.ARM_{40mT} < 10 % (Fig. 6b; Dunlop, 1983). Hence, at the low rotation rates used here transitions towards MD behaviour are shown by variability towards lower d.ARM_{40mT} with ARM_{ROT}/ARM ratios approaching ~1 (grey arrows in Figs. 6b,c). Under the experimental conditions used here, it may be that close-to-MD behaviour could also be shown as small positive Bg values (Hounslow et al., 2023). The

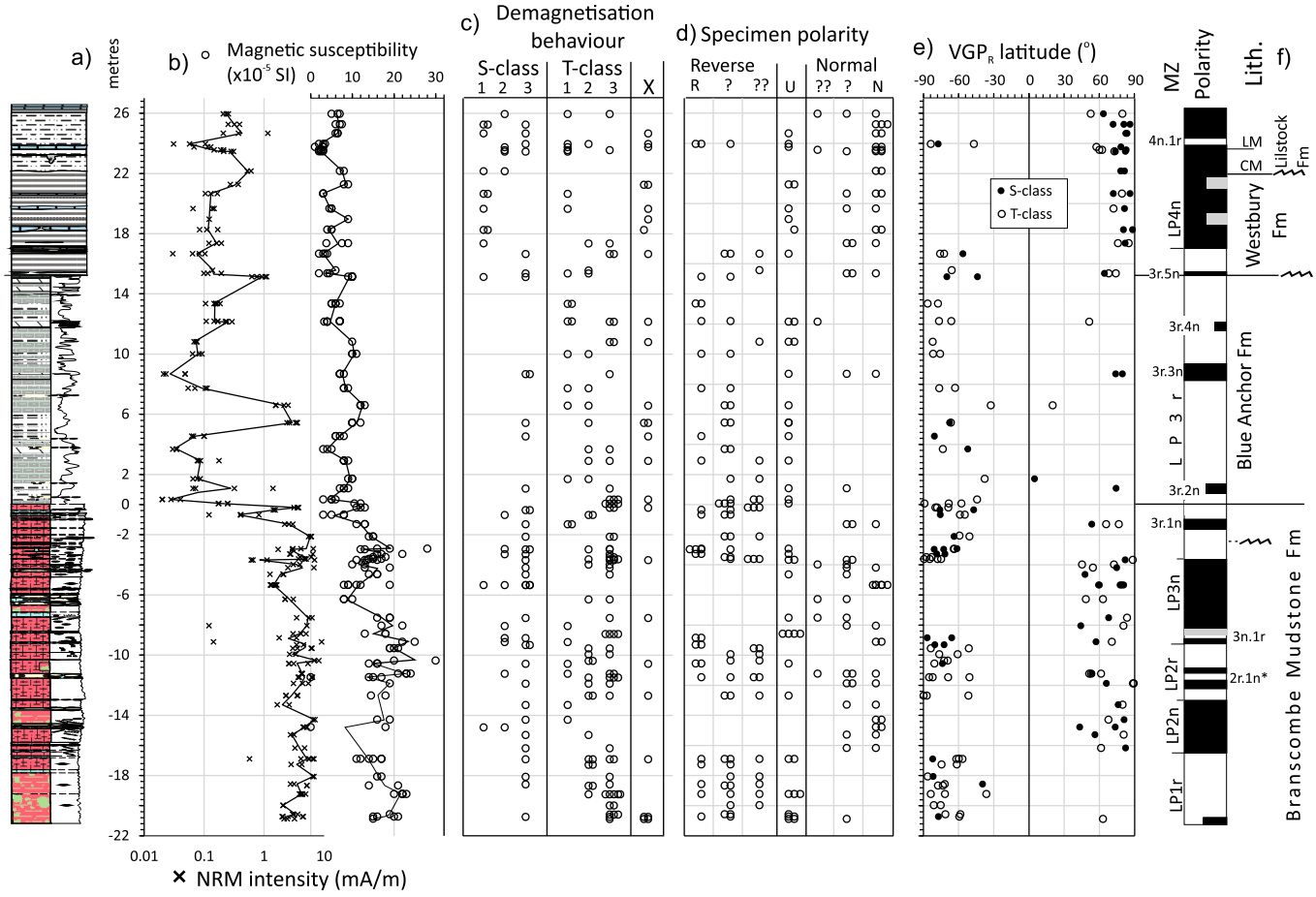

Fig. 7. Summary of petromagnetic and magnetostratigraphic data for the Lavernock section. a) simplified sedimentary log. b) NRM intensity and volumetric magnetic susceptibility, c) Demagnetisation behaviour classification of specimen data. d) Specimen polarity classification. e) Specimen virtual geomagnetic pole latitude (VGP_R) with respect to the mean poles for the Mercia Mudstone and Penarth groups. f) interpreted section polarity and lithostratigraphy. MZ = labels of magnetozone couplets (LP = Lavernock Point). LM = Langport Member, CM = Cotham Member. * on LP2r.1n indicates these two normal submagnetozones are likely a single submagnetozone, due to uncertainty in sub-section correlation at samples LP58 and LP57 (Fig. 3).

ratio of ARM_{ROT} for 2.5 Hz/0.26 Hz appears to provide an approximate proxy of magnetite particle size, with values ~0.6 indicative of SD magnetite (Chalk bacterial magnetite sample-set; Fig. 6c) and values towards ~1–1.1 indicating close-to MD-type behaviour. In this context it would appear the Penarth Group set has rather middling values, finer-grained than Mercia Mudstone Group (MMG) siliciclastics, but like the Carnian-age siliciclastics of the De Geerdalen Fm (from Svalbard). In summary, there is no evidence for a contribution from magnetic sulphides to the most stable remanence carriers in these samples, a remanence which instead is carried by fine-grained, oxidized magnetite.

4.2. Palaeomagnetic results

Creer (1957) investigated 11 MMG samples at Lavernock and inferred a composite NRM comprising a likely dual polarity shallow primary inclination component, a secondary present-day like component, and a temporary viscous component. This was inferred by comparison to a bigger set collected from near the base of the MMG at Sidmouth (SW England). This was based on undemagnetised data, but samples were stored long-term in zero field prior to measurement. Broadly, this basic inference remains unchanged with our bigger sample set, and modern instrumentation. With modern techniques, thermal demagnetisation of the red mudstones shows a wide range in NRM unblocking temperatures, with typically less than 10 % of the NRM remaining by around 600-700 °C (SI Figs. S4 - S6).

The magnetisations from our sample-set are inferred to comprise two key magnetisations. Firstly, a component (LT component) with lower stability than the primary remanence, and often evident by strong linear segments in Zijderveld plots, and often steep-downwards directions (see SI Figs. S7, S10). This component in the combined scheme was often extracted starting from the NRM (or 100-200 °C steps) to the last stages of thermal demagnetisation or early stages (5–30 mT) of AF demagnetisation (SI Fig. S8a). For thermal demagnetisation of hematite dominated specimens the LT component typically started from ~100 °C (or up to ~400 °C) with ending segment ranges up to 400-650 °C (SI Fig. S8a). In some 11 % of specimens this was the only component detected. LT component directions are quite scattered (SI Fig. S10) but have groupings near the expected Brunhes-age magnetic field (SI Fig. S10). The scatter may be caused by component overlap with temporary components and/or Triassic directions.

Secondly a dual polarity characteristic magnetisation (ChRM) inferred to be the primary Triassic magnetisation (Fig. 8). Using the thermal demagnetisation scheme, the S-class specimens have fits most frequent starting from 400 to 650 °C, with end of line segments typically to the origin, but commonly ending at 650-700 °C (SI Figs. S7, S8b). For the combined demagnetisation scheme, the start of the fitted segments ranged from thermal steps 200-350 °C or early AF (5–15 mT), and most frequently ended in the origin, but also with some ending in the 25–50 mT range (SI Fig. S8b). For the T-class specimens the great circle fits typically started from the NRM to 200 °C steps, and most frequently included the origin (SI Fig. S9).

31 % of specimens yielded S-class behaviour, with 58 % yielding T-class behaviour, with the remaining 11 % classified as X-class (Fig. 7c). The average α_{95} of the line fits for the S-class divisions (S1, S2, S3) were 7.6°, 11.2 ° and 18.1 °, and for the T-classes (T1, T2, T3) the α_{95} of the poles to the great circle planes were 16.7 °, 15.2 ° and 24.4 ° respectively. The average excess standard deviation used in LINEFIND was 1.8, indicating the average fitted error model variance is some 1.8^2 times the average measurement model variance (Kent et al., 1983).

The mean directions pass reversal tests with class Rb and Rc, and VGP dispersion is within the range ($A95_{min}$, $A95_{max}$) expected (Table 1) according to the criteria proposed by Deenen et al. (2011). The mean direction for the MMG gives a palaeopole close to other Upper Triassic poles, and elsewhere in the MMG (summary data in Hounslow and Gallois, 2023). However, the sample mean directions for the Penarth Group, are overly steep, and may be contaminated by the Brunhes-like overprint, although the overall mean direction is only 5° from the mean direction of 019/59° of Hüsing et al. (2014) from the Hettangian at St Audrie's Bay.

4.3. Magnetostratigraphy

Of the 218 specimens measured, 35 % gave normal polarity, 45 % reverse, and 20 % of specimens failing to yield unequivocal polarity (Fig. 7d). Since multiple specimens from each sample were measured, only 3 samples failed to yield polarity out of the total of 76 samples yielding specimens (six samples failed to yield any specimens; Fig. 3a).

The polarity yields four major magnetozone couplets (LP1 to LP4n), with five submagnetozones defined by a single sample (but two or more specimens), LP2r.1n, LP3n.1r, LP3r.1n, LP3r.3n, LP3r.5n and LP4n.1r (Fig. 7f). The two apparent normal magnetozones in LP2r in depth scale are likely the same magnetozone (LP2r.1n), due to uncertainty in subsection correlation across a landslip and fault, so samples LP57 and LP58 may be out of stratigraphic order (Figs. 3a, 7f). Three tentative submagnetozones, LP1r.1n, LP3r.2n and LP3r.4n are defined by single specimens (Fig. 7f). The proposed correlations between other coeval UK sections are shown in Fig. 9, with correlation to sections outside Britain discussed below. The correlations between the Seaton sections and St Audrie's are from Hounslow and Gallois (2023). The studied sequence clearly contains some erosional disconformities that segment any

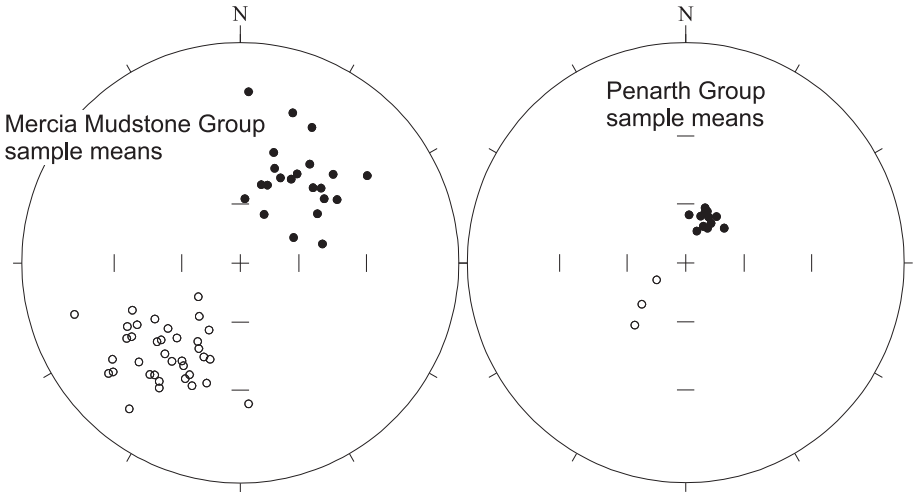

Fig. 8. Directional means for the samples from the Mercia Mudstone and Penarth groups at Lavernock.

Table 1
Directional means for the Lavernock section data (with tectonic correction), reversal tests and VGP poles. $^{+}$T-class specimens use the directions from the great circle combined mean (method of McFadden and McElhinny, 1988). $^{\$}$ = conventional Fisher mean using specimen data. N_S = number of levels (sites), N_l = number of specimens used with fitted lines, and N_p = number of specimens with great circle planes used in the determining the mean direction. α_{95}, Fisher 95 % cone of confidence. k, Fisher precision parameter. G_O is the angular separation between the inverted reverse and normal directions, and G_C is the critical value for the reversal test (McFadden and McElhinny, 1990). In the reversal test the G_O/G_C values flagged with * indicate common K values, others not flagged have statistically different K-values for reverse and normal populations, in which case a simulation reversal test was performed. Plat and Plong are the latitude and longitude of the mean virtual geomagnetic pole. A95 (min, max) = Fisher 95 % confidence interval for VGP-based site mean (N_s sites), and $A95_{min}$ and $A95_{max}$ threshold values of Deenen et al. (2011). $\%VGP_{45}$ = percent of samples yielding VGP latitude < |45|, as a reflection of the match to modern geomagnetic field models and palaeomagnetic data in which $\%VGP_{45}$ is a ~ 3–4 % (Cromwell et al., 2018). Statistics determined with Pmagtool v.5 (Hounslow, 2023).

Type/ Unit	Dec(°)	Inc(°)	k/α_{95}(°)	$N_s/N_l/N_p$	Reversal Test	G_O/G_C(°)	Plat/ Plong(°)	Dp/Dm (°)	A95 (min, max), $\%VGP_{45}$
Penarth Group									
Specimen line fits$^{\$}$	28.1	61.7	59.1	14/21/0	–	–	69.2/100	5/6.5	–
Sample mean^{+}	30.3	64.8	98.5	15/21/17	Rc	10.3/18	70/88.2	5.1/6.3	5.6 (4.1,14.9),0
Mercia Mudstone Group									
Specimen line fits$^{\$}$	44	37.1	12.5/6.2	34/46/0	Rc	5.4/10.6*	44.1/112	4.3/7.3	–
Sample mean^{+}	38.1	35.8	18.4/4.5	58/46/88	Rb	8.3/9.1*	46.6/119	3.6/6.3	4.4 (2.4,6.4), 6

magnetostratigraphic correlation, hiatuses which are well described (Mayall, 1981; Gallois, 2009), with in the case of Lavernock, an additional low angle disconformity surface some 2 m from the top of the Branscombe Mudstone Fm (below sample LP37; Fig. 3a).

4.4. Carbon isotope results

The Lavernock carbon isotope data when combined with that from Suan et al. (2012) shows a general upwards increase in $\delta^{13}C_{org}$ (Fig. 10a). Those from St Audrie's shows a similar trend, whereas those from Haven Cliff displays no trend above lower and negative $\delta^{13}C_{org}$ in the base of the sampled interval (Fig. 10b,c). When considered as whole, with respect to %TOC the $\delta^{13}C_{org}$ values show a trend to higher values with increasing %TOC (Fig. 10d). However, $\delta^{13}C_{org}$ generally are within the range expected for Late Triassic terrestrial organic matter (Dal Corso et al., 2012; Whiteside et al., 2010; Schaller et al., 2015; Bacon et al., 2011), rather than marine organic carbon (OC) since Late Triassic marine OC typically has $\delta^{13}C_{org}$ between −26 to −30 ‰ (Dal Corso et al., 2012; Williford et al., 2007; other sources in Hounslow et al., 2022b). Indeed, only a sparse marine presence can be inferred from small abundances of acritarchs and dinoflagellates in the top ~1 m of the Blue Anchor Fm at Lavernock (Orbell, 1973). More abundant marine organic matter is likely present in the Williton Mb in North Somerset sections associated with a marine macrofauna (Mayall, 1981; Warrington and Ivimey-Cook, 1995). The data from the Williton Mb at St Audrie's (Hesselbo et al., 2002; Fig. 10c), shows abruptly lower $\delta^{13}C_{org.}$ which is likely a consequence of both the hiatus across the base of the Williton Mb, and the presence of more marine OC with lower $\delta^{13}C_{org}$. In sections from North Somerset the OC source from the upper 13 m of the Blue Anchor Fm (Thomas et al., 1993) is related to %TOC such that when <~0.1 % it is dominated by plant fragments and spores, when >0.2 % TOC it has major amounts of amorphous OC (of algal origin) and/or sources from dinoflagellates, associated especially with *Rhaetogonyaulax* (Sarjeant 1963). Whilst conventionally associated with marine systems, dinoflagellates are common in freshwater, and marine forms can be tolerant of salinity changes. In essence the palaeoenvironmental significance of *Rhaetogonyaulax* is currently not fully understood (Mangerud et al., 2019).

5. Discussion

5.1. Interpretation of carbon isotope changes

The general relationship between %TOC-$\delta^{13}C_{org}$ appears to be in part related to lithology with the red mudstones having generally lower % TOC and lower $\delta^{13}C_{org}$ (red symbols in Fig. 10d). Microbially mediated respiration of organic matter could leave bulk $\delta^{13}C_{org}$ values either not much affected, or increased slightly as the nitrogenous, lower $\delta^{13}C_{org}$ organic matter is consumed (Hayes, 1983; Macko and Estep, 1984). However, refractory residual lignin, left after microbial and thermal degradation usually has lower $\delta^{13}C_{org}$ than the bulk organic matter (Benner et al., 1987), so the red mudstones may contain more refractory OC. This is to some extent borne out by the Rhaetian and Norian plant and palaeosol $\delta^{13}C_{org}$ (Richey et al., 2023), which shows on average lower $\delta^{13}C_{org}$ for woody material, and higher values for the leaf and palaeosol material (right side of Fig. 10d). Alternatively, the higher $\delta^{13}C_{org}$ in the younger intervals in the sections (grey-green mudstone; Fig. 10d) could relate to increasing abundance of algal and dinoflagellate sources (Thomas et al., 1993). The appearance of well-preserved miospores higher in the Blue Anchor Fm, may also reflect a consequential lessening in organic matter degradation. However, the mid and upper parts of the Rydon Mb at Lavernock Point and Haven Cliff have average values of ~ −24 ‰, whereas those at St Audrie's are around −22 ‰. This suggests some compositional differences in the OC between these sections, as well as additional variation, unrelated to the changes explained above. Moreover, as values <−25 ‰ are not lithology dependent, we interpret the $\delta^{13}C_{org}$ fluctuations to record a primary regional/global change signal. A more complete understanding of organic matter compositional controls over this interval awaits more detailed OC characterisation and geochemistry.

There are three (CIE-1 to 3) possible regional/global carbon isotope excursions, two centred around coeval normal magnetozones LP3r.1n ≡ HC3n ≡ SA4r.1n (≡ is used to symbolise coeval magnetozones), and a possible third just above coeval magnetozones LP3r.3n ≡ HC3r.2n, but not seen in all sections (Fig. 10). To produce a composite age-related $\delta^{13}C_{org}$ record, the data from Lavernock and St Audrie's are correlated to that at Haven Cliff using the top and base of magnetozone boundaries (Fig. 11a). In each section the $\delta^{13}C_{org}$ data were divided into a lower and an upper segment for correlation. Correlation between lower segments used the top and base of SA4n ≡ HC2n and HC3n ≡ LP3r.1n ≡ SA4r.1n for the Lavernock and St Audrie's correlations (Fig. 11a). Correlation of upper segments used the top of HC3n ≡ LP3r.1n ≡ SA4r.1n in both, and LP3r.2n at Lavernock, which also aligns submagnetozones LP3r.2n and HC3r.1n (Fig. 11a). For St Audrie's the maximum in $\delta^{13}C_{org}$ at ~ − 13 m, was matched with a similar maximum at Lavernock at ~ + 10 m (Fig. 10b, c). This approximately equated the top of the Rydon Mb at both Haven Cliff and St Audrie's. Using these correlations provides good consistency in $\delta^{13}C_{org}$ values between Haven Cliff and Lavernock, consequently a $\delta^{13}C_{org}$ curve was fitted using the combined dataset (Fig. 11a). However, the St Audrie's $\delta^{13}C_{org}$ data show deviation from that in the other sections starting at a level approximately at the base of the Blue Anchor Fm at Haven Cliff (i.e., the 0 m level; Fig. 11a), but otherwise shows fluctuations which match those from the other sections, suggesting these are at least regionally coeval. Significantly, the $\delta^{13}C_{org}$

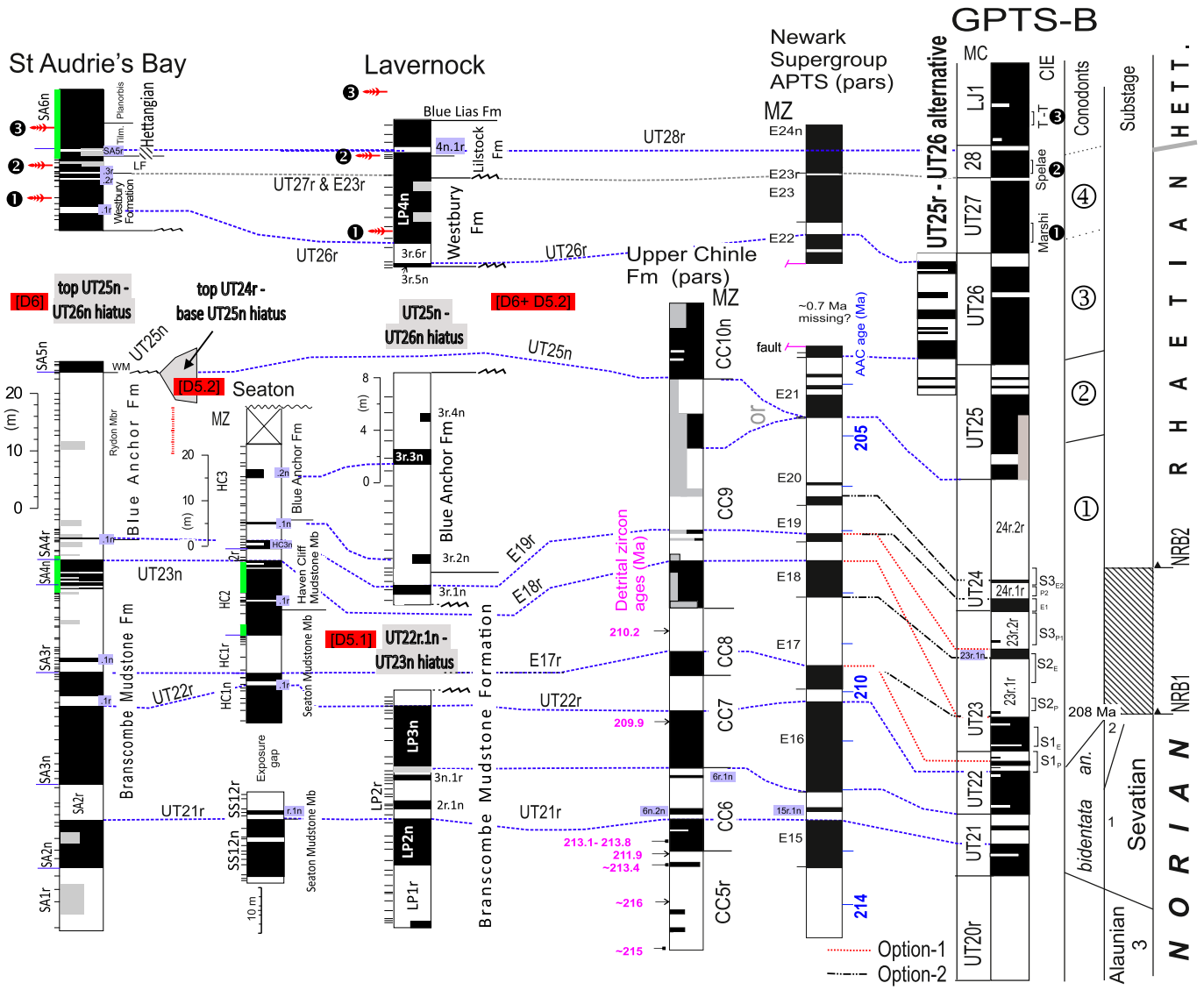

Fig. 9. Magnetostratigraphic correlation of the UK sections in the upper Branscombe Mudstone Fm, Blue Anchor Fm and Penarth Group (left three columns), and their correlation to key sections with polarity stratigraphy elsewhere. Adapted from similar summaries in Hounslow and Gallois (2023). GPTS-B = marine biochronology calibrated geomagnetic polarity scale as in Hounslow and Gallois (2023), adapted from Hounslow and Muttoni (2010). CIE column are carbon isotope excursion labels as in Figs. 2,5 and Lindström et al. (2017). T-T = Top-Tilmanni. Rhaetian 1, 2, 3, 4 are the four conodont zones for the Rhaetian as in Krystyn (2008b) and in Fig. 1b. The more recent Rhaetian conodont zones of Rigo et al. (2018), cannot be easily tied to the magnetostratigraphy, but are shown for the Sevatian (an. = *andrusovi*). Sloping boundaries in conodonts column indicates zonal boundary uncertainty with respect to the magnetochrons. Correlation options 1 and 2 as discussed in the text, and disconformity codes (red background) in UK sections (e.g. [D6]) applied from Barnasch (2009) and this work. AAC = anchored astrochronology. LF = Lilstock Fm, WM = Williton Member. (For interpretation of the references to colour in this figure legend, the reader is referred to the web version of this article.)

variations below the composite zero metre level at Haven Cliff are expressed in both red and non-red mudstones, indicating that organic matter degradation, has a limited impact on these changes (Fig. 11a).

5.2. *The Sevatian and Rhaetian interval in UK sections, role of disconformities*

The study of the Lavernock section represents the third magnetostratigraphic study from SW Britain of the interval from the upper parts of the Branscombe Mudstone Fm into the Lias Group (Fig. 9). The upper parts of the Branscombe Mudstone are of mixed polarity, the Blue Anchor Fm is dominantly reverse polarity and the Penarth and basal Lias groups dominantly normal polarity.

In the Branscombe Mudstone Fm the magnetostratigraphic correlation between the Haven Cliff section at Seaton and the St Audrie's section follows Hounslow and Gallois (2023). The correlation between the top of coeval magnetozones HC2n ≡ SA4n are particularly well defined in the uppermost part of the Branscombe Mudstone (Fig. 9). This magnetochron provides a clear correlation point into the Newark Supergroup astronomical polarity timescale (APTS), Chinle Fm and the biostratigraphic-based polarity timescale, here referred to as GTPS-B (Hounslow and Muttoni, 2010; Kent et al., 2017; Hounslow and Gallois, 2023; Wang et al., 2023; Fig. 9). Above this is the reverse polarity dominated upper-most part of the Branscombe Mudstone and the lower and mid parts of the Blue Anchor Fm (i.e. the Rydon Mb). This interval contains three (tentatively 4) brief normal magnetozones, as borne out by the consistency in the $\delta^{13}C_{org}$ change (Fig. 11a). However, insufficiently close sample spacing in some sections, and insufficient numbers of measured specimens indicate tentative (or missed) submagnetozones in some sections. Therefore, at Lavernock LP3r.1n, LP3r.2n and LP3r.3n

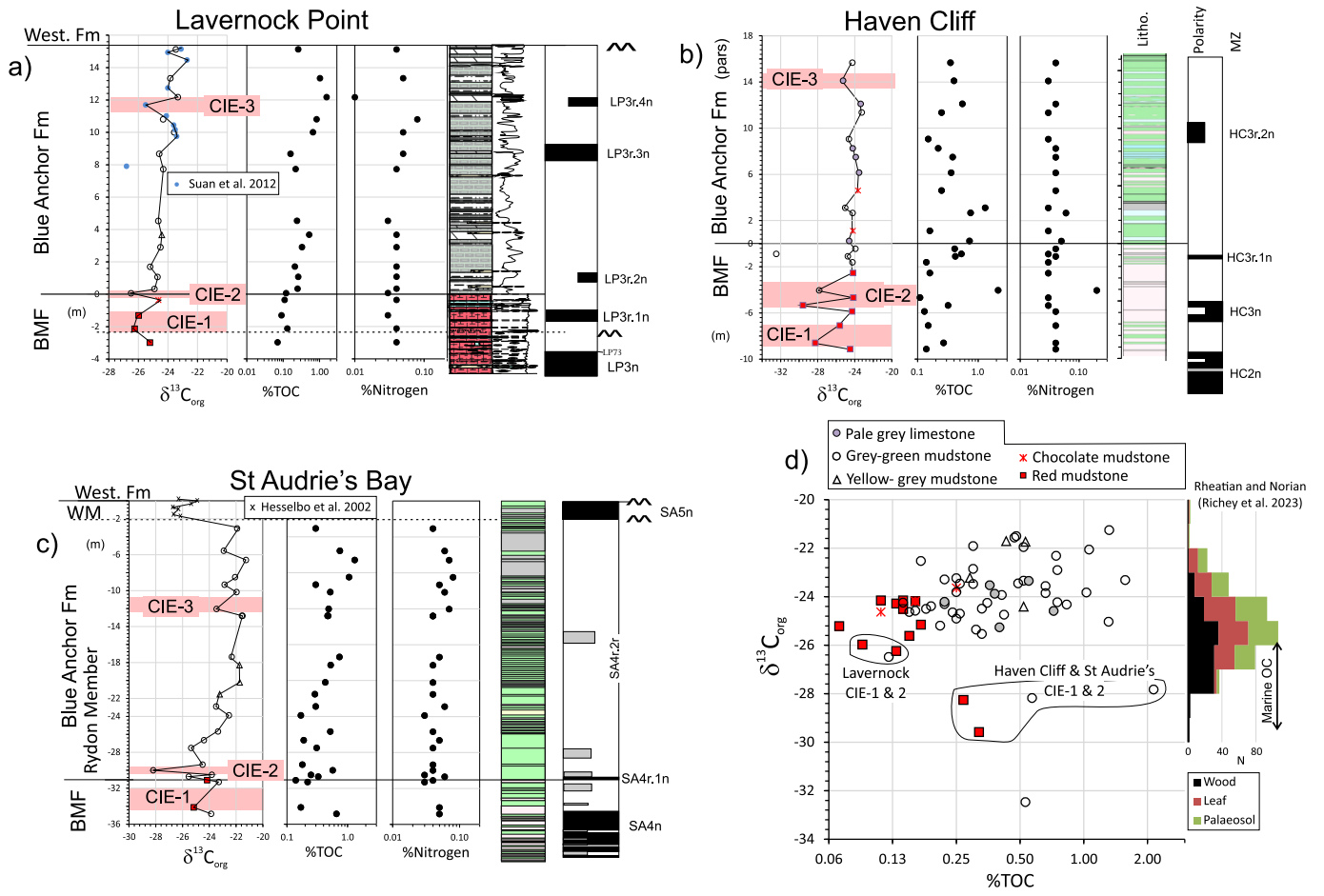

Fig. 10. a, b, c) The carbon isotope ($\delta^{13}C_{org}$), percent total organic carbon (%TOC) and percent elemental nitrogen datasets in the top parts of the MMG, with respect to the simplified logs and the magnetostratigraphy. Magnetostratigraphy for Haven Cliff and St Audrie's Bay sections from Hounslow and Gallois (2023) and Hounslow et al. (2004). $\delta^{13}C_{org}$ data are partitioned into lithology and mudstone colour (key on top of d). Additional carbon isotope data for the Williton Member from Hesselbo et al. (2002), and for Lavernock from Suan et al. (2012). CIE = Inferred possible carbon isotope excursions 1 to 3. d) All the measured $\delta^{13}C_{org}$ with respect to total organic carbon, partitioned into lithology and mudstone colour (key on top of panel). Extreme samples which fall into CIE1 and CIE2 are grouped and labelled. Right side of panel, range of Late Triassic marine and terrestrial organic matter from Richey et al. (2023), and sources listed in Hounslow et al. (2022b). BMF=Branscombe Mudstone Fm, WM = Williton Member.

are likely correlated to HC3n, HC3r.1n and HC3r.2n, respectively at Haven Cliff (Seaton composite). At St Audrie's SA4r.1n is likely coeval with HC3n at Haven Cliff, due to its presence low in magnetozone SA4r and also low in magnetozone interval HC2r-HC3r (Fig. 9).

Below SA4n ≡ HC2n in the Branscombe Mudstone are three major reverse magnetozones, well represented at St Audrie's by SA1r, SA2r and SA3r. The coeval equivalents to SA2r in the Seaton section are SS12r, and LP2r at Lavernock (Fig. 9). This reverse magnetochron contains an earlier normal submagnetochron, which is represented in the coeval interval in the Chinle Fm (i.e. CC6n.2n), Newark Supergroup (E15r.1n) and at Seaton (SS12r.1n). In the Chinle Fm, magnetozone CC6r contains an upper normal submagnetozone (CC6r.1n), which at Lavernock is considered coeval with the base of LP3n (i.e. base of LP3n.1n; Fig. 9). There is no clear representative of SA4n ≡ HC2n in the Lavernock section, and for this reason, a hiatus is inferred at the disconformity below sample LP37 (Fig. 3). Of the three sections studied from SW Britian, Lavernock is the most proximal to Mercia Mudstone lacustrine shoreline deposits (Tucker, 1977), and is therefore more likely to contain erosional hiatuses.

A disconformity at the base of the Blue Anchor Fm has also been inferred in central England, based on borehole logs (Horton et al., 1987; Old et al., 1987), and is probably coeval with that identified at Lavernock. Likewise, Barnasch (2009) correlated the Lower Exter Fm of NW Germany to the Blue Anchor Fm of the onshore succession of the Anglo-Dutch Basin, whose base is marked by the D5 disconformity (Franz et al., 2018). A similar relationship was inferred by Bachmann and Kozur (2004). The Lower Exter Fm has been divided into 2 or 3 sequences (Franz, 2008; Barnasch, 2009), with the older D5.1 disconformity transitional into the uppermost part of the Arnstadt Fm in parts of Germany (Franz, 2008; Fig. 1b). The similarity in positioning of the disconformities between the NW German Keuper and that from SW Britain is striking, and we propose that the D5.1 and D5.2 disconformities are likely expressed in those seen at Lavernock (and likely also in the English Midlands). The overlying D5.2 disconformity likely relates to that at the base of the Williton Mb (Figs. 1b, 9). The third disconformity (D5.3) proposed by Franz (2008), is not evident in the UK, and perhaps this relates to missing intervals at the base of disconformity D6 in the UK. With, the recognition of the D4 disconformity at the base of the Branscombe Mudstone Fm (Hounslow and Gallois, 2023; Fig. 1b), the striking similarity to the Triassic of the southern Permian Basin, warrants more detailed investigations of the parts missing across these disconformities, which has been a confounding issue with the German Keuper sequences (Franz et al., 2018).

5.3. *Relationship to Sevatian and early Rhaetian marine sections*

There are two options for how SA4n ≡ HC2n correlate to the GPTS-B. Option-1 is that used by Hounslow and Gallois (2023), which correlates

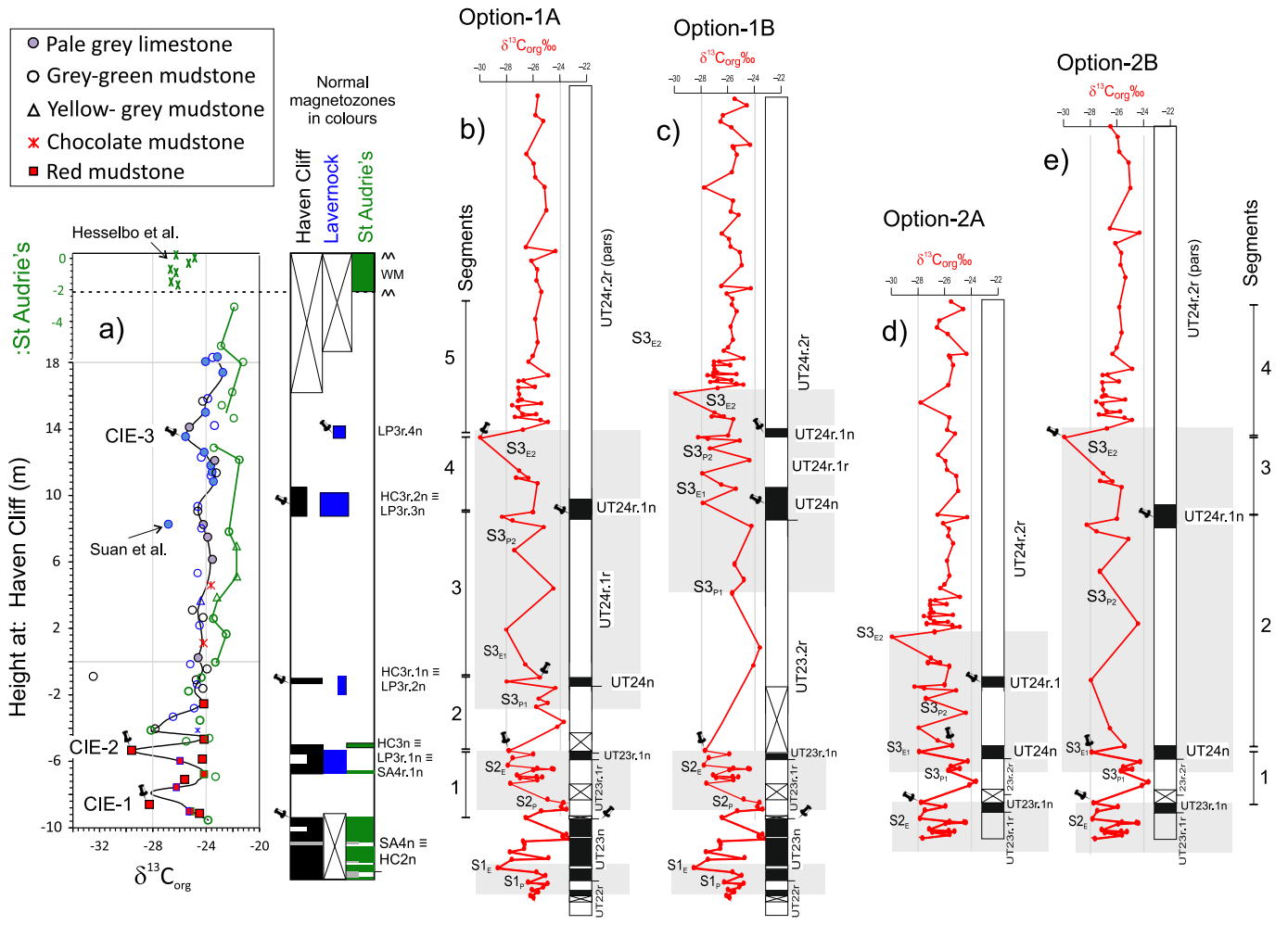

Fig. 11. a) The $\delta^{13}C_{org}$ data displayed with respect to the metre scale at the Haven Cliff section, using the magnetozone boundaries for correlation. Right panel shows position of the normal polarity magnetozone boundaries used for the Lavernock and St Audrie's data in blue and green against the correlated position of magnetozones at Haven Cliff, in black (same colours used for the perimeter of the symbols for the $\delta^{13}C_{org}$ data). The two separate pinning points used for UT23r.1n at St Audrie's (top and base of UT23r.1n at Haven Cliff) are shown as the two green normal magnetozones. The curve through the Lavernock, Haven Cliff and St Audrie's data (only below −1 m) is a loess curve (span = 0.095, using M-estimation procedure with Tukey's biweight). Columns b), c), d) and e) are the correlation options (as in text) for the Pigola Abriola $\delta^{13}C_{org}$ and polarity data, with the locations of the peaks (subscripts P, P1, P2) and negative excursions (E, E1, E2) of the isotope trends S1, S2, S3 as in Fig. 2 (with $\delta^{13}C_{org}$ using scale same as in a). The pins show the pinning points used for stretching the $\delta^{13}C_{org}$ data in each option. These mostly use the tops or mid part of the magnetozones, but also prominent lows/highs in $\delta^{13}C_{org}$ near the polarity boundaries where data gaps occur in the Pignola Abriola $\delta^{13}C_{org}$ data. (For interpretation of the references to colour in this figure legend, the reader is referred to the web version of this article.)

these magnetozones to UT23n, and by implication also E18n ≡ CC9n for the Newark and Chinle successions (red correlation lines in Fig. 9). Option-2 is that used by Kent et al. (2017) and Maron et al. (2019) which relates E18n ≡ SA4n to UT23r.1n (black correlations in Fig. 9), and by implication also HC2n and CC9n. Option-2 implies a normal submagnetochron is missing from UT23r.2r or UT24r in GPTS-B, and also from E16r in the Newark Supergroup and from CC7r in the Chinle Fm (Fig. 9). Where the missing magnetochron is placed in the interval UT23r.2r -UT24r gives rise to two alternatives for Option-2, 2A and 2B (Fig. 11d, e). How to correlate the MMG datasets to GPTS-B in this interval also gives rise to two sub-options for Option-1 (1A and 1B; Fig. 11b, c). These alternatives are assessed with the $\delta^{13}C_{org}$ data.

The Option-1 correlation implies no missing major magnetozones if correlating GPTS-B to the Newark Supergroup; which likewise applies to Option-1A for the Haven Cliff section (Table 2; Fig. 11b). There is no useful constraining biostratigraphy which favours options 1 or 2, so any confirmation comes from either the pattern of polarity changes, or the $\delta^{13}C_{org}$ around the contentious interval. The brief reverse submagnetozones in both SA4n ≡ HC2n (Fig. 9) and similar submagnetozones detected in UT23n (at Pignola Abriola and Pizzo Mondello; Fig. 12), give support to Option-1. In addition, based on anchored astrochronology datasets from Austria, NRB1 is around 208 Ma (Galbrun et al., 2020), which for Option-1 would relate to ~207.5 Ma in the Newark APTS, but for Option-2 would suggest ~209.5 Ma. Correlation Option-1 is therefore a better fit to the astrochonologies and the presence of securely known magnetozones.

Longer-range statistical similarities were also evaluated using the UT20r to UT25n interval (Table 2). This uses a statistical composite polarity scale of this interval, constructed using the method of Hounslow (2016), using the five marine section datasets with constraining conodont biostratigraphy (Fig. 12, excluding the noisier Xiquelin section data). The statistical composite is expected to average out local sedimentation rate changes from the five marine sections giving a scale with a likely closer approximation to relative duration for the magnetochrons (composite shown in GPTS-B in Fig. 9). This composite UT20r-UT25n interval was then compared to the polarity scales of the Newark Supergroup (scaled to duration as in Kent et al., 2017, table 3), and that from the Seaton and St Audrie's sections. Data from Lavernock were not used due to segmentation across the D5.1 hiatus. These comparisons generally yield larger MSI, PSI and dCor values for the Option-2

Table 2
Statistics for the comparison of the two magnetic polarity correlation models (Options 1 and 2) for the UT20r to UT25n interval. The sub-option is shown inside [] where relevant. SMI, PSI = similarity of matrices index and Procrustes similarity index (Indahl et al., 2018), and dCor = distance correlation (Székely and Rizzo, 2017), all with ranges 0–1.0 (none to perfect similarity). P_{RV} = the RV-based statistic testing the probability of association between the sets as in Josse and Holmes (2016), and P_{dCor} probability of correlation for the dCor statistic. ** <0.01, * 0.01–0.05, ⊃ >0.05 (smaller the values, greater the probability of association). d_{max} = magnetochron/ magnetozone with largest Euclidean distance. Nc = number of magnetozones/chrons in the comparison. Absent/extra = magnetozones: absent from the GPTS-B set used/ additional magnetozones in the comparison set. These are data for each variable in the dataset scaled to zero mean and 1σ. Top of Rydon Mb used as the proxy for base of UT25n; base of St Audrie's section used as proxy for base UT20r. Without 1σ scaling the intercomparison of Option-1 and 2 correlations give comparable conclusions, but the P_{RV} and P_{dCor} values for the St Audrie's correlations yield <~0.05 (See SI for data details, and R-script).

Comparison	SMI, PSI, dCor	P_{RV}, P_{dCor}	Nc, d_{max}	Absent/ extra, normal magnetozones
Option- 1				
Newark➔ GPTS-B	0.532,0.776,0.761	**,**	16, E17r ≡ UT22r.2r	none
Seaton ➔ GPTS-B [1A]	0.39, 0.648,0.672	**,**	14, HC3r.1n ≡ UT24n	none
Seaton ➔ GPTS-B [1B]	0.531, 0.686,0.661	**,*	12, HC2r ≡ UT23r.1r	/HC3r.1n
St Audrie's ➔ GTPS-B	0.524,0.535,0.635	⊃,⊃	9, SA3r ≡ UT22r.2r	UT24n, UT24r.1n /SA3r.1n
Option-2				
Newark➔ GPTS-B [2B]	0.683,0.811,0.828	**,**	14, E16n ≡ UT22n	UT22r.1n, UT23n.1r/ E20r.1n
Seaton ➔ GPTS-B [2A]	0.588,0.751,0.725	**,**	12, HC2n ≡ UT23r.1n	/HC3r.2n
Seaton ➔ GPTS-B [2B]	0.484,0.712,0.673	**,**	12, HC2n ≡ UT23r.1n	/HC3r.1n
St Audrie's ➔ GTPS-B	0.643,0.567,0.614	⊃,⊃	9, SA4r.1n ≡ UT24n	UT21r.1n, UT22r.1n, UT24r.1n/SA3r.1n

correlations, indicating a greater similarity. For the Seaton section Option-2A has the larger MSI, PSI and dCor. In the case of St Audrie's dCor is smaller for the Option-2 case. For the better of the Option-2 cases the most dissimilar magnetozones, with the largest di (referred to as d_{max}), are from non-coeval magnetozones E16n, HC2n and SA4r.1n. In the case of the better Option-1 correlations the d_{max} values belong to SA3r ≡ E17r (matched to UT22r.2r), and HC2r (matched to UT23r.1r; Fig. 11).

Additional assessment comes from of the match of the $\delta^{13}C_{org}$ stratigraphy from the MMG to the marine records, on the assumption that similarity in $\delta^{13}C_{org}$ fluctuations provides improved correlation models. Currently the possibility for linked magnetostratigraphic and $\delta^{13}C$ datasets are only feasible at Pignola Abriola and Steinbergkogel (Fig. 2). Other datasets crossing the NRB interval are described by Ward et al. (2004), Whiteside and Ward (2011), Caruthers et al. (2022), Karádi and Korte (2023) and Lei et al. (2023) but cannot be precisely related to the timeframe provided by the magnetostratigraphy. Zaffani et al. (2017) defined intervals showing trends (from $\delta^{13}C$ peaks to overlying negative excursions) in $\delta^{13}C$ over the basal Rhaetian boundary interval as trends S1, S2 and S3 (Fig. 2). Some additional data at Pignola Abriola are from Rigo et al. (2020). These $\delta^{13}C_{org}$ data are rather noisy with average deviation between samples within 10 cm of each other at 1.18 ‰. The four magnetostratigraphic correlation options relating the Pignola Abriola $\delta^{13}C_{org}$ stratigraphy to that from the MMG are shown in Fig. 11b-e. The depth scale of the Pignola Abriola $\delta^{13}C_{org}$ data were linearly-stretched to fit the correlated pinning points at magnetozone boundaries, or the middle of magnetozones. Some pinning points used $\delta^{13}C_{org}$ data values adjacent to the magnetozone boundaries (e.g. top $S2_E$, and $S3_{E1}$; Fig. 11b-e) to better accommodate unsampled intervals and matching of the $\delta^{13}C_{org}$ data points between the stretched intervals (marked with pins in Fig. 11). The statistical correlation (Pearson R value) between of the Pignola Abriola $\delta^{13}C_{org}$ data and a composite curve generated from all the MMG $\delta^{13}C_{org}$ points was also determined as an additional evaluation tool (see SI Fig. S11, Pearson R values in Fig. 13a). The $\delta^{13}C_{org}$ statistical correlation used the 4–5 segments spanning the pinning points (segments on Fig. 11b, e) for the four options in Fig. 11.

For Option-1 the peak in $\delta^{13}C_{org}$ at $S2_P$ in the early part of UT23r.1r, and a negative excursion ($S2_E$) in the later part of UT23r.1r have possible coeval features in the MMG at and below CIE-1 (Fig. 11a, b,c). The differences perhaps relate to inadequately detailed sampling in the MMG sections. The $S3_{P1}$ peak is a better match in the Option-1B model to the $\delta^{13}C_{org}$ changes in the MMG, than the Option-1 A model (segment 2; Figs. 11b,c; 13a). The excursion $S3_{E2}$ at Pignola Abriola is only really defined by a single point in $\delta^{13}C_{org}$ but by more data for $\delta^{13}C_{carb}$, which extends the excursion to higher levels in the section (Fig. 2). $S3_{E2}$ is above the uppermost normal magnetozone at Pignola Abriola (Fig. 2), yet the tentative LP3r.4n in the MMG is at or just above the CIE-3 excursion, which for Option-1B suggests LP3r.4n is spurious. For Option-1A when CIE-3 and $S3_{E2}$ are aligned these give larger R-values than for option 1B (Fig. 11b, 13a). Therefore, in spite of the reasonable match of $S3_{P1}$ in Option-1B, the Option-1A is a rather better match overall in terms of the better validated magnetozones, and their relationship to the $\delta^{13}C_{org}$. For the option-1A model, although the $\delta^{13}C_{org}$ data is sparse in UT24r.1r, it is possible excursion $S3_{E1}$ and a similar one immediately at the lower boundary of UT24r.1n may match the more minor changes seen in the MMG data (Fig. 11a,b).

For the Option-2 correlation models the $S3_{P1}$ peak in $\delta^{13}C_{org}$ is limited to the upper part of UT23r.2r, perhaps representing the positive peak in $\delta^{13}C_{org}$ between CIE-1 and CIE-2 (Fig. 11a, d,e). The $S3_{E1}$ excursion could represent CIE-2, with a short trend to larger $\delta^{13}C_{org}$ (as peak $S3_{P2}$) in Option-2A and at around −3 m in the MMG composite (Fig. 11a,d,e). The prominent excursion $S3_{E2}$ appears unrepresented in Option-2A but is coeval with CIE-3 in Option-2B (Fig. 11a,e). Also, in Option-2B the $S3_{P2}$ peak in $\delta^{13}C_{org}$ could represent the long run of larger $\delta^{13}C_{org}$ values in the MMG composite between −2 to 8 m, although the few sample points between UT24n and UT24n.1n (Fig. 11e) limit a detailed comparison. Therefore Option-2B is the preferred of the Option-2 models, also having the larger R-values (Fig. 13a).

Considering only the magnetostratigraphy, Option-1A is preferred since, 1) it has no missing or additional well-validated magnetozones (other than the tentative/spurious LP3r.4n); 2) the relative thickness and presence of minor submagnetochrons/zones in both UT23n and SA4n ≡ HC2n are a good match in the stretched records in Fig. 11a, compared to the inadequately short UT23r.1n in Option-2. In either option-1 or 2 the segment-1 is rather condensed in the MMG composite (the SA4r-SA4r.1n; HC2r- HC3n intervals) compared to Pignola Abriola, and largely visa-versa for the overlying segments (Fig. 13b). This may reflect a lateral expression of the D5.1 disconformity as seen at Lavernock, which in part covers this interval (Fig. 9), perhaps through cryptic condensed beds so far undetected in this interval. This may play a part in distorting the statistical polarity comparisons adjacent to SA4n ≡ HC2n.

Clearly a more detailed study of carbon isotopes could clarify the details adjacent to CIE-1 and CIE-2 in the UK sections. This would help consolidate the relationships in this interval, which otherwise has close sample-spacing in the Pignola Abriola section in either correlation option. A persistent feature in sections from western North America is a

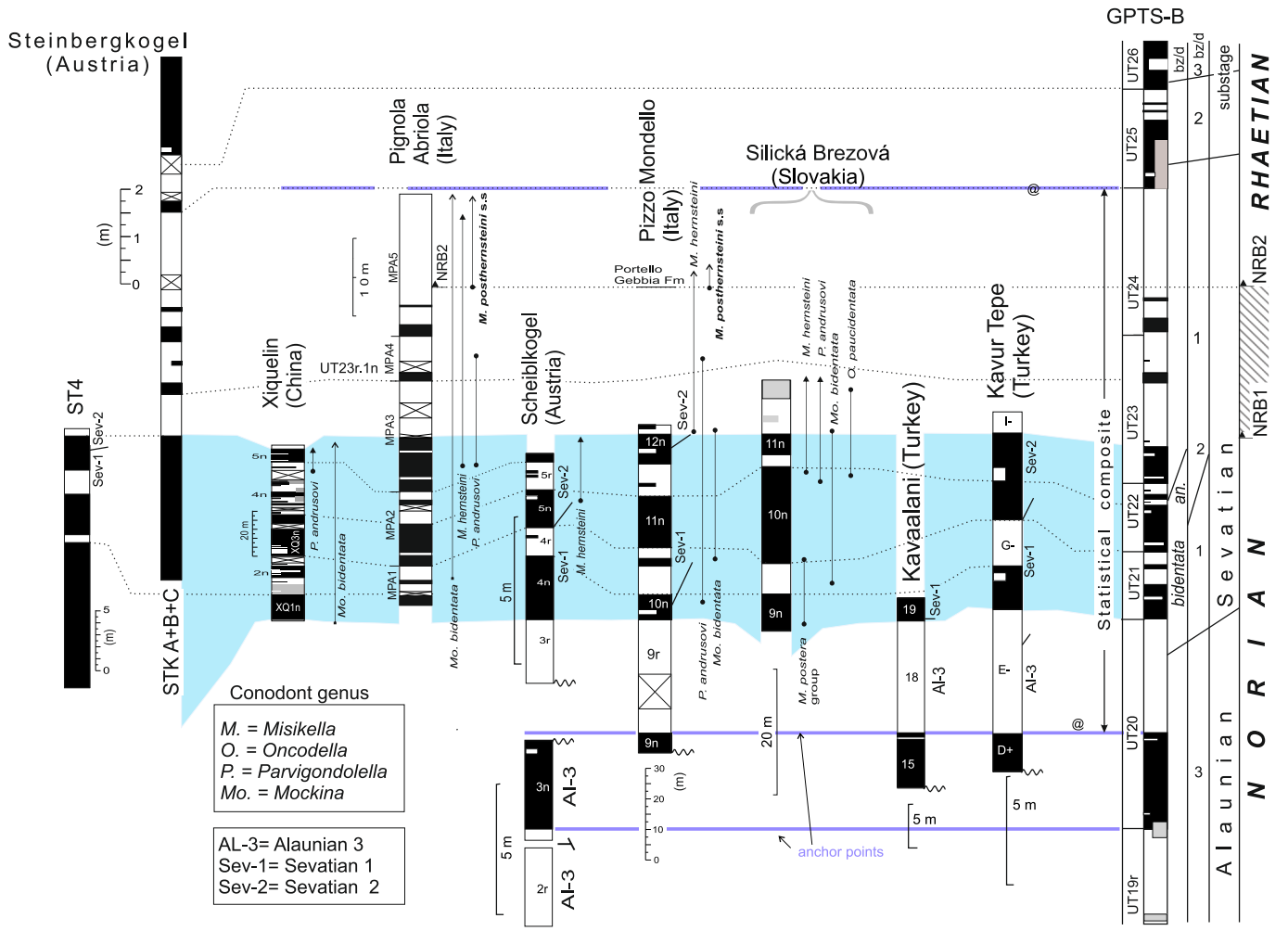

Fig. 12. Construction of the polarity composite and marine biochronology calibrated GTPTS (GTPS-B) over the Norian-Rhaetian boundary interval. In GPTS-B the interval from UT20r to UT25n is a statistical composite constructed using the method in Hounslow (2016), with the workings in the Excel spreadsheet in Hounslow (2024). This dataset is based on fig. 10 in Hounslow and Muttoni (2010), but with the addition of new data from Steinbergkogel of Hüsing et al. (2011), Pignola Abriola of Maron et al. (2015) and Bertinelli-et al. (2016) and Xiquelin from Chen et al. (2024). The key biostratigraphy for the Steinbergkogel sections is shown in Fig. 2. The two proposed options for the base of the Rhaetian are NRB1 and NRB2 (Bertinelli et al., 2016; Galbrun et al., 2020). The Sevatian conodont zones are those of Rigo et al. (2018). See Hounslow and Muttoni (2010) for other sources of other data in this figure. The Sevatian 1 and 2 subdivisions use the biostratigraphic concepts with the original magnetostratigraphic data. Conodonts at Pizzo Mondello updated from Mazza et al. (2012). @ = anchor points for composite. Bz/d = biozone or stage/substage subdivision number. Xiquelin data not used in the statistical composite.

negative carbon excursion, near the last occurrence of non-dwarf monotids (Lei et al., 2022, 2023), which may approximately relate to the position of NRB1 for the base of the Rhaetian (McRoberts et al., 2008; Krystyn et al., 2007). This broadly agrees with our data, which show more substantial (~4 ‰) excursions in $\delta^{13}C_{org}$ compared to the more minor (~2 ‰) excursion seen at the NRB2 position. Interestingly, Panthalassan sections show a possible eustatic promoted transgression close to NRB1 (Lei et al., 2022), which may relate to the transgression which brings in the Blue Anchor type facies above the red mudstones of the Branscombe Mudstone Fm. Whilst the precise relative timing of this between Panthalassan and UK sections cannot be assessed with current data, this deserves further investigation.

Many ideas on the origin of the potentially global carbon isotope excursions at around the NRB have been proposed (Jin et al., 2022; Lei et al., 2022, 2023; Chen et al., 2024), with none so far offering realistic estimates of the global volumes of carbon needed for these changes. Chaotic isotopic changes are a regular feature, as are de-coupled organic and carbonate carbon isotope records (Zaffani et al., 2017; Lei et al., 2022), and rather poor inter-section synchronicity according to biostratigraphic markers in coeval sections (Lei et al., 2023). The decoupling of organic and carbonate isotope datasets is also a feature of the Rhaetian-Hettangian boundary extinction, perhaps relating to changes in the biological community contribution to organic and carbonate producers (Yager et al., 2017), or recycling of inert organic carbon changing the $\delta^{13}C_{org}$ response (Bachan et al., 2012). Similar complexities likely relate to the NRB datasets.

The apparently poor synchronicity of CIE's at the NRB probably relates to the diachronous nature of biostratigraphic boundaries around the NRB as is evident by the biostratigraphic dating markers on Fig. 12. Some of the rather more chaotic isotopic changes could relate to variable terrestrial organic carbon sources (i.e. up to about 5 ‰ $\delta^{13}C_{org}$ differences; Fig. 10d), and for $\delta^{13}C_{carb}$ in marine successions with possible diagenetic impacts. However, substantial surface seawater temperature changes occurred in Tethys in the Sevatian to Rhaetian-1 interval, possibly promoted by mountain building of late Norian-age on the northern fringes of Tethys (Chen et al., 2024). Emplacement of a large igneous province has been hypothesised as the cause of the CIE's at the NRB (Rigo et al., 2020), but so far without substantive support on the timing or volumes of CO_2 required. An oceanic anoxic event associated with NRB2 (and the $S3_{E2}$ CIE) has also been linked to this volcanic event via CO_2 injected into the ocean/atm (Rigo et al., 2020). However, conclusive evidence for the origin of the NRB carbon cycle changes

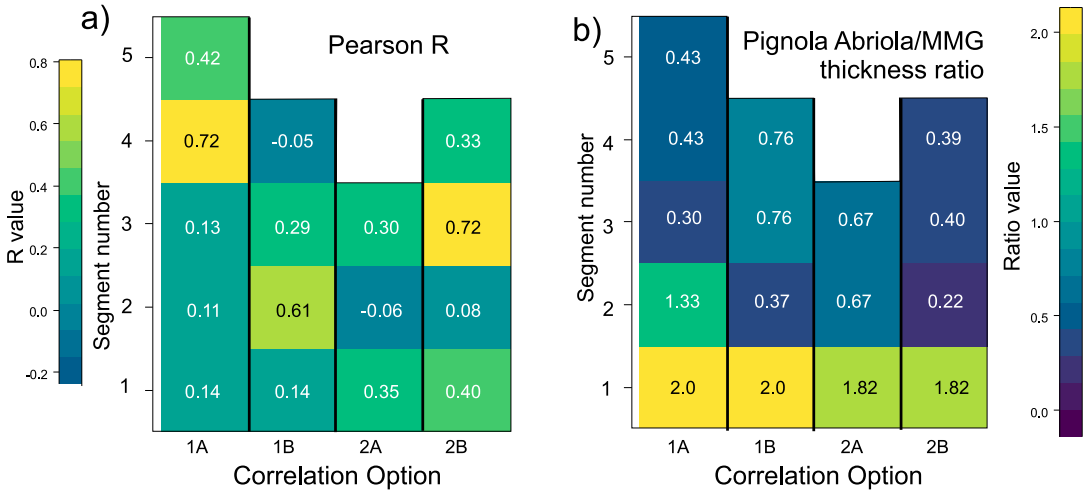

Fig. 13. Statistics displayed as 'heat maps' for the correlation options shown in Fig. 11. a) Pearson correlation coefficient (R) for Pignola Abriola $\delta^{13}C_{org}$ data points correlated to the fitted loess curve for the Mercia Mudstone Group (MMG) dataset (SI Fig. S11), broken down into the 4 to 5 segments between the base and top of the composite MMG, and the pinning points as shown in Fig. 11. b) The ratio of thickness (in metres) of the pinned segments as used in a) and shown in Fig. 11. E.g. Segment 1 (UT23r.1r + UT23r.1n in Option 1; Fig. 11b, and UT23r.2r + UT24n in Option 2; Fig. 11e) is consistently relatively thicker at Pignola Abriola, compared to overlying segments, in which the Haven Cliff section is mostly relatively thicker.

remains elusive.

5.4. The Rhaetian-Hettangian boundary interval

The Penarth Group has a pattern of polarity changes like that seen at St Audrie's (Fig. 9), although magnetozones coeval with SA5n.2r and SA5n.3r are not detected at Lavernock. A more substantive reverse magnetozone at Lavernock (LP3r.6r) in the base of the Westbury Fm, just below the Marshi CIE (Fig. 5) concurs with a similar relative positioning at St Audrie's for SA5n.1r (Hounslow et al., 2004). These reverse magnetozones are coeval with E22r ≡ UT26r (Fig. 9).

Significantly, a reverse polarity sample (magnetozone LP4n.1r) from the top of the 'White Lias' limestone interval in the Langport Mb appears to be coeval with the SA5r magnetozone at St Audrie's (Figs. 5, 9). The correlation of the Watchet Beds at Lavernock (and in South Glamorgan) has been contentious, with some suggesting they are coeval with the base of the Lias Group, based on their lithological similarity (Whittaker, 1978; Hesselbo et al., 2004; Beith et al., 2021), similar palynology (Warrington in Waters and Lawrence, 1987) and abundance of *Liostrea*. The $\delta^{13}C_{carb}$ stratigraphy places LP4n.1r within the base of the positive excursion (Korte et al., 2009; Ruhl et al., 2020), which immediately follows the Spelae CIE (Figs. 5, 9), which allows a precise correlation to SA5r at St Audrie's at the same position in the isotope stratigraphy. This is around the base of the Hettangian (Korte et al., 2019), consistent with the *Neophyllites lavernockensis* Hodges, 2021 in the 'White Lias' limestones of the Lilstock Fm at Lavernock (Hodges, 2021).

Lindström et al. (2021) have made a case that CAMP volcanism was well underway by the time of the Spelae CIE (Fig. 9). Since the CAMP volcanics studied so far are almost entirely normal polarity this must place their initiation within UT27n or more probably within UT28n, since the magnetochron UT27r ≡ E23r is persistently observed at several locations with immediately overlaying CAMP basalts (Kent et al., 2017). This places SA5r ≡ LP4n.1r within the interval occupied by the CAMP flows and intrusions, which continued through the earliest Hettangian biotic recovery (Blackburn et al., 2013). Using the timescale of Lindström et al. (2021) this would place SA5r ≡ LP4n.1r ≡ UT28r at ca. 201.35 Ma, at or below the Preakness/Holyoke basalts, and ca. 210 kyrs after the first CAMP basalts. The Holyoke Basalt was not intensely sampled in the study of the CAMP succession by Kent and Olsen (2008), and hence the equivalent of UT28r is probably still to be found in the CAMP successions in the basins of eastern North America. If the reverse magnetozone in the base of the Cotham Mb at St Audrie's (i.e. SA5n.3r) is coeval with E23r, as inferred here and by Whiteside et al. (2007); then this places the initial eruptions of the CAMP basalts in North America coeval with the basal parts of the Cotham Mb at ca. 201.56 Ma (some 3.8 m below SA5r). The duration of the first pulse of CAMP was possibly as long as ca. 120 ka (Blackburn et al., 2013), which would place the end of the first CAMP pulse at ~2.2 m above SA5n.3r, which is within the mid parts of the Langport Mb at St Audrie's, and hence the Spelae CIE relates to the mid and upper parts of the first CAMP pulse. This first pulse coincides with the two phases of rarity, and the main crisis in land plants as inferred by Lindström (2021).

6. Conclusions

Magnetostratigraphic and organic carbon isotopic data from the Lavernock section, combined with carbon isotope data from other coeval sections provide a more detailed regional understanding of the chronostratigraphy of British Upper Triassic strata, particularly that around the NRB.

The magnetic mineralogy of the samples from the Lavernock section are like that at other coeval sections, but rock magnetic measurements centred on rotational remanent magnetisation measurements demonstrate the Penarth Group remanence properties have little or no contribution from magnetic sulphides.

The magnetostratigraphy of the Lavernock section is similar to coeval sections in SW England but differs in that a hiatus is present in the late Sevatian occupied by parts of magnetochrons UT22r and UT23n. This missing interval is inferred to represent disconformity D5.1 of the German Keuper, with the overlying D5.2 disconformity equivalent to that at the base of the Williton Mb of North Somerset. The magnetochrons of Rhaetian-1 age are well represented in the topmost part of the Branscombe Mudstone Fm and Blue Anchor Fm, demonstrating the base of the Blue Anchor Fm is slightly diachronous between UK sections.

Combining the organic carbon isotope stratigraphy using coeval magnetozone boundaries from the Rhaetian-1 age sections at Lavernock, St Audrie's and Haven Cliff demonstrates a consistent pattern of isotopic changes, with three possible negative isotope excursions. With the aid of statistical evaluations, two base-types of correlation models are explored, assessing how the MMG magnetostratigraphy may correlate with that in the NRB GSSP candidate marine sections at Pignola Abriola (Italy) and Steinbergkogel (Austria). The co-occurrence of

magnetostratigraphy and carbon isotopic changes in these sections provides an additional sound framework for evaluation of these correlation models. These highlight the stronger carbon isotope excursions are located near the first occurrence of *M. posthernsteini* s.l as used at the Steinbergkogel sections, which are near coeval with the last occurrence of non-dwarf *Monotis*. The correlation model preferred based on a balance of this evidence places the NRB (using the older *M. posthernsteini* s.l definition, NRB1) in the uppermost few metres of the Branscombe Mudstone Fm. The younger candidate definition of the NRB (using the *M. posthernsteini* s.s definition, NRB2) places it in the upper parts of the Blue Anchor Fm, adjacent to a less pronounced, negative excursion, best seen at Lavernock with the current sampling density (Fig. 11a). Clear-cut evidence for the origin of the NRB carbon isotope excursions changes remain elusive, but they are expressed in the British terrestrial successions, which suggests global character.

At Lavernock the equivalent to the St Audrie's magnetozone SA5r (≡ UT28r) is detected in the 'White Lias' limestone of the Langport Mb, close to the occurrence of *Neophyllites lavernockensis.* This magnetozone postdates the Spelae carbon isotope excursion and is located at the base of the positive carbon isotope excursion probably marking the base of the Hettangian. The coeval equivalent to UT26r is also detected in the Westbury Fm at Lavernock, prior to the Marshi carbon isotope excursion which is in magnetochron UT27n of Rhaetian-4 age. Correlation of these to CAMP bearing successions, highlights the near coeval occurrence of the initial CAMP basalts and the base of the Cotham Mb of the Lilstock Fm, within the end Triassic extinction interval of Lindström et al. (2017).

CRediT authorship contribution statement

Mark W. Hounslow: Writing – original draft, Visualization, Validation, Software, Resources, Project administration, Methodology, Investigation, Funding acquisition, Formal analysis, Data curation, Conceptualization. **Julian E. Andrews:** Writing – original draft, Visualization, Validation, Project administration, Investigation, Funding acquisition, Conceptualization.

Declaration of competing interest

The authors declare that they have no known competing financial interests or personal relationships that could have appeared to influence the work reported in this paper.

Data availability

All data from work is either available in the Supplementary Information, or available on the figshare data repository (Hounslow, 2024).

Acknowledgements

This work was supported by Leverhulme Trust grant F/204/W. Magnetic measurements were also performed by Gregg McIntosh, Mengyu Hu, Seth Morgan and Vassil Karloukovski. Palaeomagnetic sample preparation was by Paulette Posen, with field assistance from Paulette Posen and Alan Kendal. Isotope sample preparations were performed by David Mindham, with isotope measurements by David Hughes at Lancaster. Reviews by Giovanna Della Porta and Giovanni Muttoni improved this work.

Appendix A. Supplementary data

Supplementary figures to this article can be found online at https://doi.org/10.1016/j.palaeo.2024.112579.

References

Bachan, A., van de Schootbrugge, B., Fiebig, J., McRoberts, C.A., Ciarapica, G., Payne, J. L., 2012. Carbon cycle dynamics following the end-Triassic mass extinction: Constraints from paired $\delta^{13}C_{carb}$ and $\delta^{13}C_{org}$ records. Geochem. Geophys. Geosyst. 13. https://doi.org/10.1029/2012GC004150.

Bachmann, G.H., Kozur, H.W., 2004. The Germanic Triassic: correlations with the international chronostratigraphic scale, numerical ages and Milankovitch cyclicity. Hallesches Jahrbuch für Geowissenschaften 26, 17–62.

Bachmann, G.H., Geluk, M.C., Warrington, G., Becker-Roman, A., Beutler, G., Hagdorn, H., Hounslow, M.W., Nitsch, E., Röhling, H.-G., Simon, T., Szulc, A., 2010. Triassic. In: Doornenbal, J.C., Stevenson, A.G. (Eds.), Petroleum Geological Atlas of the Southern Permian Basin Area. EAGE Publications, Houten, pp. 149–173.

Bacon, K.L., Belcher, C.M., Hesselbo, S.P., Mcelwain, J.C., 2011. The Triassic–Jurassic boundary carbon-isotope excursions expressed in taxonomically identified leaf cuticles. Palaios 26, 461–469. https://doi.org/10.2110/palo.2010.p10-120r.

Barnasch, J., 2009. Der Keuper im Westteil des Zentraleuropäischen Beckens (Deutschland, Niederlande, England, Dänemark): diskontinuierliche Sedimentation, Litho-, Zyklo-und Sequenzstratigraphie. PhD Thesis,. Univ of Halle (Salle).

Barth, G., Franz, M., Heunisch, C., Ernst, W., Zimmermann, J., Wolfgramm, M., 2018. Marine and terrestrial sedimentation across the T–J transition in the North German Basin. Palaeogeogr. Palaeoclimatol. Palaeoecol. 489, 74–94.

Beith, S.J., Fox, C.P., Marshall, J.E., Whiteside, J.H., 2021. Recurring photic zone euxinia in the northwest Tethys impinged end-Triassic extinction recovery. Palaeogeogr. Palaeoclimatol. Palaeoecol. 584. https://doi.org/10.1016/j.palaeo.2021.110680.

Beith, S.J., Fox, C.P., Marshall, J.E., Whiteside, J.H., 2023. Compound-specific carbon isotope evidence that the initial carbon isotope excursion in the end-Triassic strata in northwest Tethys is not the product of CAMP magmatism. Glob. Planet. Chang. 222. https://doi.org/10.1016/j.gloplacha.2023.104044.

Benner, R., Fogel, M.L., Sprague, E.K., Hodson, R.E., 1987. Depletion of ^{13}C in lignin and its implications for stable carbon isotope studies. Nature 329 (6141), 708–710.

Bertinelli, A., Casacci, M., Concheri, G., Gattolin, G., Godfrey, L., Katz, M.E., Maron, M., Mazza, M., Mietto, P., Muttoni, G., Rigo, M., 2016. The Norian/Rhaetian boundary interval at Pignola-Abriola section (Southern Apennines, Italy) as a GSSP candidate for the Rhaetian Stage: an update. Albertiana 43, 5–18.

Blackburn, T.J., Olsen, P.E., Bowring, S.A., McLean, N.M., Kent, D.V., Puffer, J., McHone, G., Rasbury, E.T., Et-Touhami, M., 2013. Zircon U-Pb geochronology links the end-Triassic extinction with the Central Atlantic Magmatic Province. Science 340 (6135), 941–945.

Boomer, I., Copestake, P., Raine, R., Azmi, A., Fenton, J.P., Page, K.N., O'Callaghan, M., 2021. Stratigraphy, palaeoenvironments and geochemistry across the Triassic–Jurassic boundary transition at Carnduff, County Antrim, Northern Ireland. Proc. Geol. Assoc. 132, 667–687.

Briden, J.C., Arthur, G.R., 1981. Precision of measurement of remanent magnetization. Can. J. Earth Sci. 18, 527–538.

Brodie, C.R., Leng, M.J., Casford, J.S., Kendrick, C.P., Lloyd, J.M., Yongqiang, Z., Bird, M. I., 2011. Evidence for bias in C and N concentrations and $\delta^{13}C$ composition of terrestrial and aquatic organic materials due to pre-analysis acid preparation methods. Chem. Geol. 282, 67–83.

Caruthers, A.H., Marroquín, S.M., Gröcke, D.R., Golding, M.L., Aberhan, M., Them II, T. R., Veenma, Y.P., Owens, J.D., McRoberts, C.A., Friedman, R.M., Trop, J.M., 2022. New evidence for a long Rhaetian from a Panthalassan succession (Wrangell Mountains, Alaska) and regional differences in carbon cycle perturbations at the Triassic-Jurassic transition. Earth Planet. Sci. Lett. 577. https://doi.org/10.1016/j.epsl.2021.117262.

Chen, Y., Zeng, W., Joachimski, M.M., Wignall, P.B., Ogg, J.G., Jiang, H., Zhang, M., Lai, X., 2024. Late Triassic (Norian) strontium and oxygen isotopes from the Baoshan block, southwestern China: possible causes and implications for climate change. Palaeogeogr. Palaeoclimatol. Palaeoecol. 650, 112378. https://doi.org/10.1016/j.palaeo.2024.112378.

Creer, K.M., 1957. V. The remanent magnetization of unstable Keuper Marls. Philos. Trans. Royal Soc. London. Series A, Math. Phys. Sci. 250, 130–143.

Cromwell, G., Johnson, C.L., Tauxe, L., Constable, C.G., Jarboe, N.A., 2018. PSV10: a global data set for 0–10 Ma time-averaged field and paleosecular variation studies. Geochem. Geophys. Geosyst. 19, 1533–1558.

Dal Corso, J., Mietto, P., Newton, R.J., Pancost, R.D., Preto, N., Roghi, G., Wignall, P.B., 2012. Discovery of a major negative δ13C spike in the Carnian (late Triassic) linked to the eruption of Wrangellia flood basalts. Geology 40, 79–82. https://doi.org/10.1130/G32473.1.

Deenen, M., Langereis, C., Krijgsman, W., Hachimi, H.E., Chellai, E.H., 2011. Palaeomagnetic results from Upper Triassic red-beds and CAMP lavas of the Argana Basin, Morocco. In: Van Hinsbergen, D.J.J., Buiter, S.J.H., Torsvik, T.H., Gaina, C., Webb, S.J. (Eds.), The Formation and Evolution of Africa: A Synopsis of 3.8 Ga of Earth History, 357. Geological Society, London, Special Publications, pp. 195–209. https://doi.org/10.1144/SP357.10.

Dunlop, D.J., 1983. Determination of domain structure in igneous rocks by alternating field and other methods. Earth Planet. Sci. Lett. 63, 353–367.

Falkingham, P.L., Maidment, S.C., Lallensack, J.N., Martin, J.E., Suan, G., Cherns, L., Howells, C., Barrett, P.M., 2022. Late Triassic dinosaur tracks from Penarth, South Wales. Geol. Mag. 159, 821–832.

Franz, M., 2008. Litho-und leitflächenstratigraphie, chronostratigraphie, zyklo-und sequenzstratigraphie des Keupers im östlichen Zentraleuropäischen Becken (Deutschland, Polen) und Dänischen Becken (Dänemark, Schweden). PhD thesis,. Univ. Halle (Saale).

Franz, M., Bachmann, G.H., Barnasch, J., Heunisch, C., Röhling, H.-G., 2018. Der Keuper in der Stratigraphischen Tabelle von Deutschland 2016 –kontinuierliche

Sedimentation in der norddeutschen Beckenfazies (Variante B). Z. Dt. Ges. Geowiss. 169, 203–224.
Galbrun, B., Boulila, S., Krystyn, L., Richoz, S., Gardin, S., Bartolini, A., Maslo, M., 2020. " Short" or "long" Rhaetian? Astronomical calibration of Austrian key sections. Glob. Planet. Chang. 192. https://doi.org/10.1016/j.gloplacha.2020.103253.
Gallois, R.W., 2007. The stratigraphy of the Penarth Group (late Triassic) of the East Devon coast. Geosci. South-West England 11, 287–297.
Gallois, R.W., 2009. The lithostratigraphy of the Penarth Group (late Triassic) of the Severn Estuary area. Geoscience in South-West England. Proc. Ussher Soc. 12, 71–84.
Geluk, M.C., 2005. Stratigraphy and Tectonics of Permo-Triassic Basins in the Netherlands and Surrounding Areas. PhD thesis,. Utrecht University.
Hartley, N., Shuttleworth, P., 2024. Girl Discovers Dinosaur Footprints on Beach Walk. https://www.bbc.co.uk/news/articles/c049pe7gx6do.
Hayes, J.M., 1983. Practice and principles of isotopic measurements in organic geochemistry. In: Meinschein, W.G. (Ed.), Organic Geochemistry of Contemporaneous and Ancient Sediments, Great Lakes Section of the Society of Economic Paleontologists and Mineralogists, pp. 5–31.
Hesselbo, S.P., Robinson, S.A., Surlyk, F., Piasecki, S., 2002. Terrestrial and marine extinction at the Triassic-Jurassic boundary synchronized with major carbon-cycle perturbation: a link to initiation of massive volcanism? Geology 30, 251–254.
Hesselbo, S.P., Robinson, S.A., Surlyk, F., 2004. Sea-level change and facies development across potential Triassic–Jurassic boundary horizons, SW Britain. J. Geol. Soc. Lond. 161, 365–379.
Hodges, P., 2021. A new ammonite from the Penarth Group, South Wales and the base of the Jurassic System in SW Britain. Geol. Mag. 158, 1109–1114.
Horton, A., Poole, E.G., Williams, B.J., Illing, V.C., Hobson, G.D., 1987. Geology of the country around Chipping Norton. In: Memoir, British Geological Survey, Sheet 218. HMSO, England and Wales.
Hounslow, M.W., 1985. Magnetic fabric arising from paramagnetic phyllosilicate minerals in mudrocks. J. Geol. Soc. Lond. 142, 995–1006.
Hounslow, M.W., 2016. Geomagnetic reversal rates following Palaeozoic superchrons have a fast restart mechanism. Nat. Commun. 7. https://doi.org/10.1038/ncomms12507.
Hounslow, M.W., 2023. Palaeomag-Tools, Version 5.1a. Figshare. [Software]. https://doi.org/10.6084/m9.figshare.24167190.v1.
Hounslow, M.W., 2024. The Lavernock Point magnetic, carbon isotope and chronostratigraphic datasets [dataset]. https://doi.org/10.6084/m9.figshare.25942678.v1.
Hounslow, M.W., Gallois, R., 2023. Magnetostratigraphy of the Mercia Mudstone Group (Devon, UK): implications for regional relationships and chronostratigraphy in the Middle to late Triassic of western Europe. J. Geol. Soc. Lond. 180. https://doi.org/10.1144/jgs2022-173.
Hounslow, M.W., Muttoni, G., 2010. The geomagnetic polarity timescale for the Triassic: linkage to stage boundary definitions. In: Lucas, S.G. (Ed.), The Triassic Timescale, 334. Geological Society, London, Special Publications, pp. 61–102.
Hounslow, M.W., Ruffell, A., 2006. In: Brenchly, P.J., Rawson, P.F. (Eds.), Triassic-Seasonal Rivers, Dusty Deserts and Salty Lakes. Geology of England and Wales, Geological Society of London Publication, pp. 295–324.
Hounslow, M.W., Posen, P.E., Warrington, G., 2004. Magnetostratigraphy and biostratigraphy of the Upper Triassic and lowermost Jurassic succession, St. Audrie's Bay, UK. Palaeogeogr. Palaeoclimatol. Palaeoecol. 213, 331–358.
Hounslow, M.W., Xuan, C., Nilsson, A., 2022a. Chapter 5: Using the geomagnetic field for correlation and dating. In: Coe, A.L. (Ed.), Deciphering Earth's History: The Practice of Stratigraphy. Geological Society of London, pp. 81–99.
Hounslow, M.W., Harris, S.E., Karloukovski, V., Mørk, A., 2022b. Geomagnetic polarity and carbon isotopic stratigraphic assessment of the late Carnian -earliest Norian in Svalbard: evidence for a major hiatus and improved Boreal to Tethyan correlation. Nor. J. Geol. 102, 202204, 10.17850/njg102-1-4.
Hounslow, M.W., Horng, C.S., Karloukovski, V., 2023. Rotational remanent magnetization as a magnetic mineral diagnostic tool at low rotation rates. Geophys. J. Int. 232, 300–321.
Hüsing, S.K., Deenen, M.H., Koopmans, J.G., Krijgsman, W., 2011. Magnetostratigraphic dating of the proposed Rhaetian GSSP at Steinbergkogel (Upper Triassic, Austria): Implications for the late Triassic time scale. Earth Planet. Sci. Lett. 302, 203–216.
Hüsing, S.K., Beniest, A., van der Boon, A., Abels, H.A., Deenen, M.H.L., Ruhl, M., Krijgsman, W., 2014. Astronomically-calibrated magnetostratigraphy of the lower Jurassic marine successions at St. Audrie's Bay and East Quantoxhead (Hettangian–Sinemurian; Somerset, UK). Palaeogeogr. Palaeoclimatol. Palaeoecol. 403, 43–56.
Indahl, U.G., Næs, T., Liland, K.H., 2018. A similarity index for comparing coupled matrices. J. Chemom. 32. https://doi.org/10.1002/cem.3049.
Ivimey-Cook, H.C., 1962. On the Relationship between the Fauna and the Sediments of the Rhaetic of South-East Glamorgan. PhD thesis. University College, Cardiff.
Ivimey-Cook, H.C., 1974. The Permian and Triassic deposits of Wales. In: Owen, T.R. (Ed.), The Upper Palaeozoic and Post Palaeozoic Rocks of Wales. University of Wales Press.
Jin, X., Ogg, J.G., Lu, S., Shi, Z., Kemp, D.B., Hua, X., Onoue, T., Rigo, M., 2022. Terrestrial record of carbon-isotope shifts across the Norian/Rhaetian boundary: a high-resolution study from northwestern Sichuan Basin, South China. Glob. Planet. Chang. 210. https://doi.org/10.1016/j.gloplacha.2022.103754.
Josse, J., Holmes, S., 2016. Measuring multivariate association and beyond. Stat. Surveys 10, 132–167. https://doi.org/10.1214/16-SS116.
Karádi, V., Korte, C., 2023. Upper Carnian to Rhaetian (Upper Triassic) conodont and carbon-isotope stratigraphy of the Csővár borehole succession, Hungary. Palaeogeogr. Palaeoclimatol. Palaeoecol. 630. https://doi.org/10.1016/j.palaeo.2023.111792.
Kent, D.V., Olsen, P.E., 2008. Early Jurassic magnetostratigraphy and paleolatitudes from the Hartford continental rift basin (eastern North America): Testing for polarity bias and abrupt polar wander in association with the Central Atlantic magmatic province. J. Geophys. Res. Solid Earth 113 (B6). https://doi.org/10.1029/2007JB005407.
Kent, J.T., Briden, J.C., Mardia, K.V., 1983. Linear and planar structure in ordered mulivariate data as applied to progressive demagnetisation of palaeomagnetic remanence. Geophys. J. R. Astron. Soc. 81, 75–87.
Kent, D.V., Olsen, P.E., Muttoni, G., 2017. Astrochronostratigraphic polarity time scale (APTS) for the late Triassic and early Jurassic from continental sediments and correlation with standard marine stages. Earth Sci. Rev. 166, 153–180.
Korte, C., Hesselbo, S.P., Jenkyns, H.C., Rickaby, R.E., Spötl, C., 2009. Palaeoenvironmental significance of carbon-and oxygen-isotope stratigraphy of marine Triassic–Jurassic boundary sections in SW Britain. J. Geol. Soc. Lond. 166, 431–445.
Korte, C., Ruhl, M., Palfy, J., Ullmann, C.V., Hesselbo, S.P., 2019. Chemostratigraphy across the Triassic-Jurassic boundary. In: Sial, A.N., Gaucher, C., Ramkumar, M., Ferreira, V.P. (Eds.), Chemostratigraphy across Major Chronological Boundaries. Geophysical Monograph 240. American Geophysical Union, John Wiley, pp. 185–210.
Krystyn, L., 2008a. Excursion 1. The Hallstatt pelagics – Norian and Rhaetian Fossillagerstaetten of Hallstatt. Berichte der Geologischen Bundesanstalt 76, 81–98.
Krystyn, L., 2008b. An ammonoid-calibrated Tethyan conodont time scale of the late Upper Triassic. Berichte der Geologischen Bundesanstalt 76, 9–11.
Krystyn, L., 2010. Decision report on the defining event for the base of the Rhaetian stage. Albertiana 38, 11–12.
Krystyn, L., Richoz, S., Gallet, Y., Bouquerel, H., Kürschner, W.M., Spötl, C., 2007. Updated bio-and magnetostratigraphy from Steinbergkogel (Austria), candidate GSSP for the base of the Rhaetian stage. Albertiana 36, 164–173.
Laborde-Casadaban, M., Homberg, C., Schnyder, J., Borderie, S., Raine, R., 2021. Do soft sediment deformations in the late Triassic and early Jurassic of the UK record seismic activity during the break-up of Pangea? Proc. Geol. Assoc. 132, 688–701.
Lei, J.Z., Golding, M.L., Husson, J.M., 2022. Paleoenvironmental interpretation of the Late Triassic Norian–Rhaetian boundary interval in the Whitehorse Trough (Stikine Terrane, northern Canadian Cordillera). Palaeogeogr. Palaeoclimatol. Palaeoecol. 608. https://doi.org/10.1016/j.palaeo.2022.111306.
Lei, J.Z., Husson, J.M., Golding, M.L., van Wieren, C.S., Orchard, M.J., Caruthers, A.H., Carter, E.S., 2023. Late Triassic carbon isotope anomalies in the Canadian Cordillera: Paleoenvironmental disturbances associated with the Norian/Rhaetian boundary and end-Triassic mass extinction event. Available at SSRN:. https://doi.org/10.2139/ssrn.4666610.
Lindström, S., 2021. Two-phased mass rarity and extinction in land plants during the end-Triassic climate crisis. Front. Earth Sci. 9. https://doi.org/10.3389/feart.2021.780343.
Lindström, S., Erlström, M., 2006. The late Rhaetian transgression in southern Sweden: Regional (and global) recognition and relation to the Triassic–Jurassic boundary. Palaeogeogr. Palaeoclimatol. Palaeoecol. 241, 339–372.
Lindström, S., van De Schootbrugge, B., Hansen, K.H., Pedersen, G.K., Alsen, P., Thibault, N., Dybkjær, K., Bjerrum, C.J., Nielsen, L.H., 2017. A new correlation of Triassic–Jurassic boundary successions in NW Europe, Nevada and Peru, and the Central Atlantic Magmatic Province: a time-line for the end-Triassic mass extinction. Palaeogeogr. Palaeoclimatol. Palaeoecol. 478, 80–102.
Lindström, S., Callegaro, S., Davies, J., Tegner, C., van De Schootbrugge, B., Pedersen, G. K., Youbi, N., Sanei, H., Marzoli, A., 2021. Tracing volcanic emissions from the Central Atlantic Magmatic Province in the sedimentary record. Earth Sci. Rev. 212. https://doi.org/10.1016/j.earscirev.2020.103444.
Lucas, S.G., 2023. Imprecision and instability of the Phanerozoic chronostratigraphic scale: a solution. Evolv. Earth 1. https://doi.org/10.1016/j.eve.2023.100011.
Lucas, S.G., Tanner, L.H., 2018. The missing mass extinction at the Triassic-Jurassic boundary. In: Tanner, L.H. (Ed.), The Late Triassic World: Earth in a Time of Transition, pp. 721–785.
Macko, S.A., Estep, M.L., 1984. Microbial alteration of stable nitrogen and carbon isotopic compositions of organic matter. Org. Geochem. 6, 787–790.
MacQuaker, J.H.S., 1994. Palaeoenvironmental significance of 'bone-beds' in organic-rich mudstone successions: an example from the Upper Triassic of south-West Britain. Zool. J. Linnean Soc. 112, 285–308.
Magee, J.W., Bowler, J.M., Miller, G.H., Williams, D.L.G., 1995. Stratigraphy, sedimentology, chronology and palaeohydrology of Quaternary lacustrine deposits at Madigan Gulf, Lake Eyre, South Australia. Palaeogeogr. Palaeoclimatol. Palaeoecol. 113, 3–42.
Maher, B.A., Karloukovski, V.V., Mutch, T.J., 2004. High-field remanence properties of synthetic and natural submicrometre haematites and goethites: significance for environmental contexts. Earth Planet. Sci. Lett. 226, 491–505.
Mahon, S.W., Stephenson, A., 1997. Rotational remanent magnetization (RRM) and its high temporal and thermal stability. Geophys. J. Int. 130, 383–389.
Man, O., 2008. On the identification of magnetostratigraphic polarity zones. Stud. Geophys. Geod. 52, 173–186.
Mander, L., Twitchett, R.J., Benton, M.J., 2008. Palaeoecology of the late Triassic extinction event in the SW UK. J. Geol. Soc. Lond. 165, 319–332.
Mangerud, G., Paterson, N.W., Riding, J.B., 2019. The temporal and spatial distribution of Triassic dinoflagellate cysts. Rev. Palaeobot. Palynol. 261, 53–66.
Maron, M., Rigo, M., Bertinelli, A., Katz, M.E., Godfrey, L., Zaffani, M., Muttoni, G., 2015. Magnetostratigraphy, biostratigraphy, and chemostratigraphy of the Pignola-

Abriola section: New constraints for the Norian-Rhaetian boundary. GSA Bull. 127, 962–974.
Maron, M., Muttoni, G., Rigo, M., Gianolla, P., Kent, D.V., 2019. New magnetobiostratigraphic results from the Ladinian of the Dolomites and implications for the Triassic geomagnetic polarity timescale. Palaeogeogr. Palaeoclimatol. Palaeoecol. 517, 52–73.
Marzoli, A., Bertrand, H., Knight, K.B., Cirilli, S., Buratti, N., Vérati, C., Nomade, S., Renne, P.R., Youbi, N., Martini, R., Allenbach, K., 2004. Synchrony of the Central Atlantic magmatic province and the Triassic-Jurassic boundary climatic and biotic crisis. Geology 32 (11), 973–976.
Mayall, M.J., 1981. The late Triassic Blue Anchor Formation and the initial Rhaetian marine transgression in south-West Britain. Geol. Mag. 118, 377–384.
Mazza, M., Rigo, M., Gullo, M., 2012. Taxonomy and biostratigraphic record of the Upper Triassic conodonts of the Pizzo Mondello section (western Sicily, Italy), GSSP candidate for the base of the Norian. Riv. Ital. Paleontol. Stratigr. 118, 85–130.
McFadden, P.L., McElhinny, M.W., 1988. The combined analysis of remagnetisation circles and direct observations in paleomagnetism. Earth Planet. Sci. Lett. 87, 161–172.
McFadden, P.L., McElhinny, M.W., 1990. Classification of the reversal test in paleomagnetism. Geophys. J. Int. 103, 725–729.
McKie, T., 2014. Climatic and tectonic controls on Triassic dryland terminal fluvial system architecture, Central North Sea. In: Martinius, A.W., Ravnås, R., Howell, J.A., Steel, R.J., Wonham, J.P. (Eds.), Depositional Systems to Sedimentary Successions on the Norwegian Continental Margin. Wiley and Sons, International Association of sedimentologists, pp. 19–57.
McRoberts, C.A., Krystyn, L., Shea, A., 2008. Rhaetian (late Triassic) Monotis (Bivalvia: Pectinoida) from the eastern Northern Calcareous Alps (Austria) and the end-Norian crisis in pelagic faunas. Palaeontology 51, 721–735.
Old, R.A., Sumbler, M.G., Ambrose, K., 1987. Geology of the country around Warwick. In: Memoir British Geological Survey, Sheet 184. HMSO, England & Wales.
Olson, P., Hinnov, L.A., Driscoll, P.E., 2014. Nonrandom geomagnetic reversal times and geodynamo evolution. Earth Planet. Sci. Lett. 388, 9–17.
Orbell, G., 1973. Palynology of the British Rhaeto-Liassic. Bull. Geol. Surv. Great Brit. 44, 1–39.
Potter, D.K., Stephenson, A., 1986. The detection of fine particles of magnetite using anhysteretic and rotational remanent magnetizations. Geophys. J. Int. 87, 569–582.
R Core Team, 2022. R: A Language and Environment for Statistical Computing. R Foundation for Statistical Computing, Vienna, Austria. https://www.R-project.org/.
Richardson, L., 1905. The Rhaetic and contiguous deposits of Glamorganshire. Q. J. Geol. Soc. 61, 385–424.
Richey, J.D., Nordt, L., White, J.D., Breecker, D.O., 2023. Isoorg23: an updated compilation of stable carbon isotope data of terrestrial organic materials for the cenozoic and mesozoic. Earth Sci. Rev. 241. https://doi.org/10.1016/j.earscirev.2023.104439.
Rigo, M., Bertinelli, A., Concheri, G., Gattolin, G., Godfrey, L., Katz, M.E., Maron, M., Mietto, P., Muttoni, G., Sprovieri, M., Stellin, F., 2016. The Pignola-Abriola section (southern Apennines, Italy): a new GSSP candidate for the base of the Rhaetian Stage. Lethaia 49, 287–306.
Rigo, M., Mazza, M., Karádi, V., Nicora, A., 2018. New Upper Triassic conodont biozonation of the Tethyan realm. In: Tanner, L. (Ed.), The Late Triassic World. Springer, Cham, pp. 189–235. https://doi.org/10.1007/978-3-319-68009-5_6.
Rigo, M., Onoue, T., Tanner, L.H., Lucas, S.G., Godfrey, L., Katz, M.E., Zaffani, M., Grice, K., Cesar, J., Yamashita, D., Maron, M., 2020. The Late Triassic Extinction at the Norian/Rhaetian boundary: Biotic evidence and geochemical signature. Earth Sci. Rev. 204. https://doi.org/10.1016/j.earscirev.2020.103180.
Rizzi, M., Thibault, N., Ullmann, C.V., Ruhl, M., Olsen, T.K., Moreau, J., Clémence, M.E., Mette, W., Korte, C., 2020. Sedimentology and carbon isotope stratigraphy of the Rhaetian Hochalm section (late Triassic, Austria). Glob. Planet. Chang. 191. https://doi.org/10.1016/j.gloplacha.2020.103210.
Ruhl, M., Hesselbo, S.P., Al-Suwaidi, A., Jenkyns, H.C., Damborenea, S.E., Manceñido, M.O., Storm, M., Mather, T.A., Riccardi, A.C., 2020. On the onset of Central Atlantic Magmatic Province (CAMP) volcanism and environmental and carbon-cycle change at the Triassic–Jurassic transition (Neuquén Basin, Argentina). Earth Sci. Rev. 208. https://doi.org/10.1016/j.earscirev.2020.103229.
Schaller, M.F., Wright, J.D., Kent, D.V., 2015. A 30 Myr record of late Triassic atmospheric pCO_2 variation reflects a fundamental control of the carbon cycle by changes in continental weathering. GSA Bull. 127, 661–671. https://doi.org/10.1130/B31107.1.
Snowball, I.F., 1997. The detection of single-domain greigite (Fe_3S_4) using rotational remanent magnetization (RRM) and the effective gyro field (Bg): mineral magnetic and palaeomagnetic applications. Geophys. J. Int. 130, 704–716.
Suan, G., Föllmi, K.B., Adatte, T., Bomou, B., Spangenberg, J.E., Schootbrugge, B.V.D., 2012. Major environmental change and bonebed genesis prior to the Triassic–Jurassic mass extinction. J. Geol. Soc. Lond. 169, 191–200.
Székely, G.J., Rizzo, M.L., 2017. The energy of data. Ann. Rev. Stat. Appl. 4, 447–479.
Thomas, J.B., Marshall, J., Mann, A.L., Summons, R.E., Maxwell, J.R., 1993. Dinosteranes (4, 23, 24-trimethylsteranes) and other biological markers in dinoflagellate-rich marine sediments of Rhaetian age. Org. Geochem. 20, 91–104.
Tucker, M.E., 1977. The marginal Triassic deposits of South Wales: continental facies and palaeogeography. Geol. J. 12, 169–188.
Wang, M., Li, M., Kemp, D.B., Landwehrs, J., Jin, Z., 2023. Late Triassic sedimentary records reveal the hydrological response to climate forcing and the history of the chaotic Solar System. Earth Planet. Sci. Lett. 607. https://doi.org/10.1016/j.epsl.2023.118052.
Ward, P.D., Garrison, G.H., Haggart, J.W., Kring, D.A., Beattie, M.J., 2004. Isotopic evidence bearing on late Triassic extinction events, Queen Charlotte Islands, British Columbia, and implications for the duration and cause of the Triassic/Jurassic mass extinction. Earth Planet. Sci. Lett. 224, 589–600.
Warrington, G., Ivimey-Cook, H.C., 1995. The late Triassic and early Jurassic of coastal sections in West Somerset and south and mid-Glamorgan. In: Taylor, P.D. (Ed.), Field Geology of the British Jurassic. Geological Society of London, London, pp. 9–30.
Waters, R.A., Lawrence, D.J.D., 1987. Geology of the South Wales Coalfield, Part III, the country around Cardiff. In: Memoir British Geological Survey, Sheet 263, 3rd edition. HMSO, England and Wales.
Watkins, N.D., Haggerty, S.E., 1967. Primary oxidation variation and petrogenesis in a single lava. Contrib. Mineral. Petrol. 15, 251–271.
Whiteside, J.H., Ward, P.D., 2011. Ammonoid diversity and disparity track episodes of chaotic carbon cycling during the early Mesozoic. Geology 39, 99–102.
Whiteside, J.H., Olsen, P.E., Kent, D.V., Fowell, S.J., Et-Touhami, M., 2007. Synchrony between the Central Atlantic magmatic province and the Triassic–Jurassic mass-extinction event? Palaeogeogr. Palaeoclimatol. Palaeoecol. 244, 345–367.
Whiteside, J.H., Olsen, P.E., Eglinton, T., Brookfield, M.E., Sambrotto, R.N., 2010. Compound specific carbon isotopes from Earth's largest flood basalt eruptions directly linked to the end-Triassic mass extinction. Proc. Natl. Acad. Sci. 107, 6721–6725. https://doi.org/10.1073/pnas.1001706107.
Whittaker, A., 1978. The lithostratigraphical correlation of the uppermost Rhaetic and lowermost Liassic strata of the W Somerset and Glamorgan areas. Geol. Mag. 115, 63–67.
Wignall, P.B., 2001. Large igneous provinces and mass extinctions. Earth Sci. Rev. 53 (1–2), 1–33.
Williford, K.H., Ward, P.D., Garrison, G.H., Buick, R., 2007. An extended organic carbon-isotope record across the Triassic–Jurassic boundary in the Queen Charlotte Islands, British Columbia, Canada. Palaeogeogr. Palaeoclimatol. Palaeoecol. 244, 290–296. https://doi.org/10.1016/j.palaeo.2006.06.032.
Wilson, R.L., Lomax, R., 1972. Magnetic remanence related to slow rotation of ferromagnetic material in alternating magnetic fields. Geophys. J. Int. 30, 295–303.
Yager, J.A., West, A.J., Corsetti, F.A., Berelson, W.M., Rollins, N.E., Rosas, S., Bottjer, D.J., 2017. Duration of and decoupling between carbon isotope excursions during the end-Triassic mass extinction and Central Atlantic Magmatic Province emplacement. Earth Planet. Sci. Lett. 473, 227–236.
Yager, J.A., West, A.J., Thibodeau, A.M., Corsetti, F.A., Rigo, M., Berelson, W.M., Bottjer, D.J., Greene, S.E., Ibarra, Y., Jadoul, F., Ritterbush, K.A., 2021. Mercury contents and isotope ratios from diverse depositional environments across the Triassic–Jurassic Boundary: Towards a more robust mercury proxy for large igneous province magmatism. Earth Sci. Rev. 223. https://doi.org/10.1016/j.earscirev.2021.103775.
Zaffani, M., Agnini, C., Concheri, G., Godfrey, L., Katz, M., Maron, M., Rigo, M., 2017. The Norian "chaotic carbon interval": new clues from the $\delta^{13}C_{org}$ record of the Lagonegro Basin (southern Italy). Geosphere 13, 1133–1148.
Zaffani, M., Jadoul, F., Rigo, M., 2018. A new Rhaetian $\delta^{13}C_{org}$ record: carbon cycle disturbances, volcanism, end-Triassic mass extinction. Earth Sci. Rev. 178, 92–104.